2011

Graphene Based Rf/microwave Impedance Sensing and Low Loss Conductor for RF Applications

Iramnaaz Iramnaaz
Wright State University

GRAPHENE BASED RF/MICROWAVE IMPEDANCE SENSING & Low Loss conductor for RF applications.

A thesis submitted in partial fulfillment of the requirements for the degree of Master of Science in Engineering.

By

Iramnaaz Iramnaaz.

B.Tech, Jawaharlal Nehru Technological University, INDIA, 2008.

2011

Wright State University.

WRIGHT STATE UNIVERSITY

SCHOOL OF GRADUATE STUDIES

June 21, 2011

I HEREBY RECOMMEND THAT THE THESIS PREPARED UNDER MY SUPERVISION BY Iramnaaz Iramnaaz ENTITLED GRAPHENE BASED RF/MICROWAVE IMPEDANCE SENSING and Low Loss conductor for RF applications. BE ACCEPTED IN PARTIAL FULFILLMENT OF THE REQUIREMENTS FOR THE DEGREE OF Master of Science in Engineering.

_____

Yan Zhuang, Ph.D.

Thesis Director.

_____

Kefu Xue, Ph.D., Chair

Department of Electrical Engineering

Committee on Final Examination:

_____

Dr. Yan Zhuang, Ph.D.

_____

Dr. Kuan-Lun-Chu, Ph.D.

_____

Dr. Saiyu Ren, Ph.D.

_____

Andrew Hsu, Ph.D.

Dean, School of Graduate Studies.

Abstract

Iramnaaz, Iramnaaz. M.S.Egr., Department of Electrical Engineering, Wright State University, 2011. GRAPHENE BASED RF/MICROWAVE IMPEDANCE SENSING and Low Loss conductor for RF applications.

Biosensors are becoming more popular recently and expanding due to their broad applications in detecting disease and infectious agents, monitoring of environmental toxins, etc. Recognition and quantification of biochemical molecules and molecular interactions present great challenges in biosensing [38]. Impedance sensing at radio frequency (RF) /microwave frequency becomes very attractive as bio-molecules exhibits large distinct dielectric properties, and also because the ionic conductivity of water in most physiological systems is greatly diminished. For example, it has been reported that tumoral cells exhibits large value of electrical conductivity and permittivity which can result in significant variation of the impedance when compared to the normal cells [38].

The dynamic processes occurring in several microscopic, mesoscopic, and macroscopic organisms play key roles in device sensing and can be effectively monitored by impedance characterization. Graphene and its derivatives have attracted much attention recently for their application in biological sensing systems because of their unique 2D structure, flat planar surface and electronic properties. In this thesis, we made use of on-chip integrated impedance bio-sensors using coplanar waveguides (CPWs) as the sensing platform. Absorption of chemicals like Chitosan and DNA on graphene (or) graphene derivatives lead to remarkable red-shift of the resonant frequencies [38]. Substrate complex permittivity has been extracted from the simulation by using the ADS (Advanced design system) software. The imaginary part of the permittivity indicated significant leakage currents in the graphene/graphene derivatives, Chitosan, and DNA [38].

In this thesis, a proof-concept of transmission line based RF/microwave frequency has been reported for impedance bio-/chemical-sensor. The results showed that adding biomolecules to graphene oxide coated CPW sensors caused significant red-shift in the resonance frequency and the decrease of the resistance of the resonant frequencies, reflecting the change of the complex permittivity of the attached biomolecules. The experimental results obtained have also been verified by performing the 2D simulation [38].

On the other hand low loss conductors can be used and easily integrated with the high speed electronic circuits. They are basically used to overcome the drawback caused due to interconnect RC delay and also to improve the passive components present on the circuit. Earlier devices occupied more area and increased the cost of the system. Low ferromagnetic frequency (FMR), eddy current loss, magnetic loss etc, caused the poor quality factor inspite of adding thin ferromagnetic films like "$Ni_{80}Fe_{20}$" [35].The interconnect RC delay causes drawbacks such as low speed, energy dissipation, signal integrity etc which become more severe as we move to higher generation of technology (35 nm).

Low loss artificial conductor based on ARLYM superlattice is being used to improve the passive components present on the circuit and also to overcome the issue with RC delay [35]. Thus, this approach of using the low loss artificial conductor method is been used for demonstrating the on-chip inductors having high quality factor and can be easily used for high speed electronics.

Thus, this approach is proved to be very effective based on artificial layered material consisting of layers of "$Ni_{80}Fe_{20}$" (or) "Cu" superlattice [35]. By adjusting the thickness between the two layers the skin effect can be reduced to a great extent by using the high saturation material named "FeCo" to a minimum frequency [35].

Advisor: Dr. Yan Zhuang.

Table of Contents: - Pgs.

List of Figures:

List of Tables:

ACKNOWLEDGEMENT:

First of all, I would like to thank Dr. Yan Zhuang, my thesis advisor for his continuous support and guidance throughout my thesis. His motivation, expertise and research ideas made me progress in the right direction. I would try my best to live upto his expectations in future work. I would also like to thank Dr. Saiyu Ren and Dr. Kuan-Lun-Chu who were kind enough to accept the invitation and serve as the thesis committee members. I would like to express my sincere thanks and respect to Dr. Kumar Yelamarthi for the support and guidance provided. Without him this research would not have been possible. I would like to thank the Department of Electrical Engineering, Wright state university for their support throughout my study period.

I would like to use this opportunity to thank Dr. Kefu Xue for his constant motivation and encouragement. I would also like to thank him as he inspired me to do research. I would also like to thank my family and friends for their support and belief they had in me. Without their encouragement and belief this would have not been possible. I hope I can live up to their expectations.

Dedicated to

My family, friends &

Colleagues.

CHAPTER-1:

1.1 INTRODUCTION:

Biosensors have been studied for past several years and large amount of work has been done in this field for the last fifty years. The first era of biosensing was recognized by Clark in 1962 with his invention of "glucose enzyme electrode" [44].

Biosensors are becoming more popular today due their applications in detection of disease, infectious agents, and monitoring of environmental toxins, etc [38]. Recognition and quantification of biochemical molecules and molecular interactions present great challenges in biosensing [38]. Current biosensing methods can be classified into two categories:-

(1) Direct-labeling and (2) label-free techniques [38].

Direct-labeling technique involves methods like radioactive, fluorescent, chemiluminescence, colormetric etc [38]. This method makes use of attaching the label to improve the signal generation and also has advantage in detecting new targets due to capture of only one antibody per target. But there are also some disadvantages to this method as it involves lot of cost and additional time [21].

As a result, label-free approach is being more acceptable due to reduction in cost and it has also improved the accuracy. The complexity due to labeling is also reduced by using this method of sensing and it allows the platform for real-time measurement. There are basically four techniques which can be adopted for label free operation they are plasmonic, photonic, electronic, and mechanical [38]. Among all the above methods we made use of the SPR method in our approach.

Surface plasmonic resonance (SPR) is a label free method which is very sensitive to the surface. It has also been used for several areas like optics to get the optical properties and refractive index while the formation of protein complex [23]. SPR is also applicable to very thin such as nanometer scale films so we use this method for bio-sensing in RF frequency applications. Therefore, both sensitivity and selectivity can be achieved [32].

Sensitivity, selectivity, fast response time, and cost are the major factors considered for sensing implementation. The dynamic processes occurring in microscopic, mesoscopic, and macroscopic organisms play key role in device sensing and can be effectively monitored by impedance characterization [38]. The main advantage of impedance sensing over other sensing mechanisms is it can measure even small changes occurring by providing a large change in the impedance. It has great potential to combine both selectivity and sensitivity. Therefore it can also be useful for sophisticated applications, rapid measurement with a small volume of samples [38].

Impedance sensing in radio frequency (RF) /microwave frequency regime (MHz to GHz) becomes very attractive, in part because it makes use of the signal transduction mechanism based on its sensitivity by monitoring the changes in the physical properties, changes occurred near the surface of the substrate confined, size and shape. Bio-molecules exhibit rather large and distinct dielectric properties, and in part because the ionic contributed conductivity of water in most physiological systems is greatly diminished. For instance, it has been reported that tumoral cells exhibit larger values of electrical conductivity and permittivity than normal cells, which results in the significant variation of impedance [38]. This allows direct label free sensing of the target molecules in their native physiologic environment. Though impedance sensing is very reliable for RF measurement but suffers a major drawback of unclear specificity and sensitivity [38].

Therefore, we make use of chemical (nano-materials) reagents in this approach to implement sensitivity and selectivity and we also can distinguish the chemicals easily from the obtained response operated at different frequencies. For example one kind of response observed is by absorption of nano materials on the surface. Therefore, we focus on the nano materials and their properties (section 1.2) to improve the sensing mechanism.

1.2 Nano materials:

Nanomaterials can be defined as the materials with unique properties and having the range of several nanometers length [1]. Nanomaterials have large surface area and are very sensitive to chemical agents so they are widely being used in sensing applications. The large surface area helps in binding of the molecules to the surface and it increases the rate of the reaction. Several different chemicals can be used and tested on its surface due to the sensitive nature. Thus, we can improve both sensitivity and selectivity by using nanomaterials for sensing [10].In our approach we made use of different nanomaterials (Graphene, Chitosan and DNA) for sensing to overcome the drawback of impedance sensing. Some of the nanomaterials like carbon nanotubes and graphene have become very popular due to their properties and they provide large surface area for sensing [18, 1].

1.3 Carbon Nanotubes (CNTs):

Carbon nanotubes have very small size and structure. It has a one-dimensional structure in the shape of cylinder as shown in the fig-1.3 [25]. Due to very small size and good performance they can also be used for biosensors [19]. They are very reliable compared to Cu interconnects.

1.3.1 Structure of CNTs:

CNTs has the structure of the cylinder which is made of graphene sheets [13].Based on the structure CNTs are divided into two types, single walled CNTs and Multiple walled CNTs [36]. The single walled CNT consist of one single sheet having width of several nanometer whereas the multiple walled CNTs has several sheets covered on top of each other with different diameters of each sheet [13]. The single walled CNTs can be developed using chemical vapor deposition technique and some other methods like laser vaporization can also be used [30].SWCNTs and MWCNTs can behave like metal or a semiconductor depending on the thickness [1].

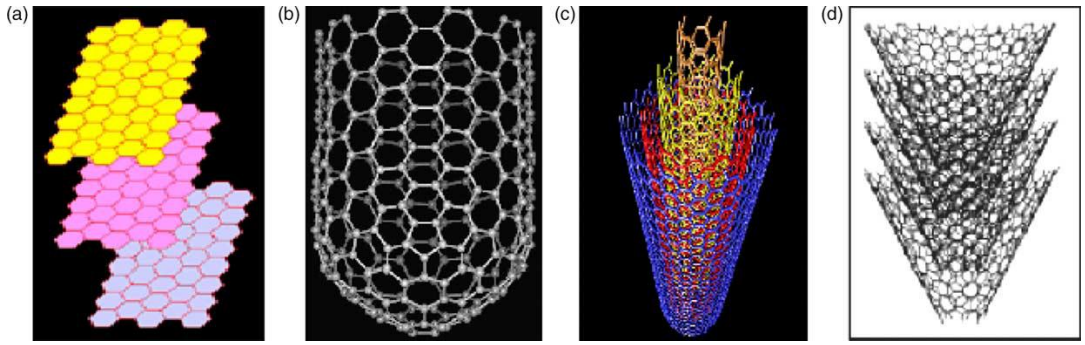

Fig1.3: "Schematic illustration of CNTs: (a) carbon nano-walls; (b) arm-chair type metallic SWNT (10, 10); (c) structure of multiwalled nanotube; and (d) structure of a four-nanocone-stacked CNF" [6].

Carbon nanotubes can be used for some sensing applications due to their unique shape, stability and high electronic properties in solutions [16]. The disadvantage of CNTs is the synthesis and purification is difficult due to formation of other additional compounds like carbon and some other particles along with CNTs which requires extra effort to separate the CNTs from other compounds which increases the complexity [18]. The other dis-advantage is seen in electrochemical application when carbon nanotubes are mixed with acids and leads to breaking

of ends which increases the solubility of CNTs [1, 13]. CNTs also has lower resistivity when compared to other interconnects [13].

SWCNT has cylindrical structure which looks like the form of a tube where each atom is connected with the nanowire on its surface. Similarly, MWCNTs consists of several sheets which are symmetrical [8].Therefore, this structure of CNTs which are connected with the nanowires helps in sensing ability.

1.3.2 Advantages of CNTs:

Carbon nanotubes has small compact size and provides larger surface area for sensing application. The high conductivity and electronic properties of CNTs helps to improve the faster rate of reaction in biosensors [12]. CNTs also offer additional advantage such as high surface to volume ratio, large storage capability and they have higher reliability. Therefore, they have been widely used for the designing of sensors recently. CNTs also offer faster response time at very low cost and higher sensitivity [12]. Additionally we can also measure the change in resistivity value and measure several other parameters like permittivity and dielectric constant using CNTs.

1.3.3 Disadvantages of CNTs:

- It's time consuming and expensive to extract molecules and synthesis.
- Difficult to maximize the adsorption of particles.
- CNTs provide only one output response at a time and limits the impedance sensing mechanism
- We can only monitor the change in DC resistance.

- Above all the major drawback using CNTs is we cannot planarize the device due to its complex tube structure.

Huge amount of work has been published on change in resistance in CNTs by attaching bio-chemical agents at its surface. But most of the measurements were performed at lower frequencies and does not contain any information about the reactance formed by the adsorption of chemical agents at the surface and cannot be used at higher frequency [19]. Therefore, CNTs are not ideal for impedance sensing due to the complexity involved thus we switch to another nanomaterial named graphene.

1.4 Graphene based impedance sensing:

Graphene is a 2-dimensional material which has thickness of single atomic layer. It is a carbon material in the form of a sheet bonded by carbon atoms in the form of lattice. Graphene structure has sp2 bonded carbon atoms and is a very new material which came into existence recently in 2004. Graphene also exists in different states such as “buckyballs” which has spherical shape like a ball and is zero dimensional. In addition to that graphene can also available in one-dimensional form such as the carbon nanotubes (CNTs) [22]. Above all the most popular form of graphene is available in the form of graphene oxide which is formed when the graphene sheet contacts with air and gets oxidized which further undergoes the process of reduction before being used. Therefore, due to the unique planar structure and physical properties graphene is being widely studied in several technological fields.

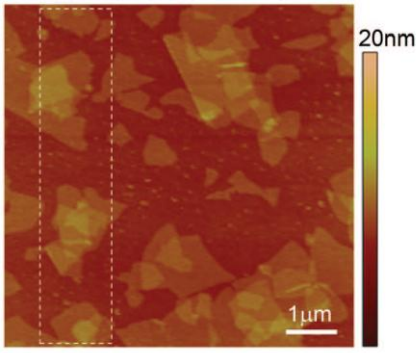

Fig: 1.4: "AFM image of the GO films where mono, bi, and trilayers of GO films can be identified" [43].

Inspite of the short history graphene is being widely being applied for several applications because of its high sensitivity compared to other materials like nanotubes and nanowires. The crystalline nature of graphene and its unique electronic properties are the main reason for the widespread recognition. Graphene can be produced in large quantity at a very low cost which provides greater advantage over the carbon nanotubes [27]. Compared to the complex process involved in developing the CNTs, graphene can be produced from the graphite which is cheaply available [4].Graphene provides a very flat surface which is very suitable for planarizing the device. Therefore, we made use of GO in our method.

In this work, we designed the coplanar waveguides (CPWs) for sensing as the on-chip integrated impedance biosensors as they provide larger surface area for sensing and using the chemical reagents which can be adsorbed easily on the flat surface. Therefore, we made use of graphene, chitosan and DNA in our method and studied the effects produced by adsorbing each of the chemicals on the surface in a systematic manner.

We noted that by directly dropping the DNA onto the surface containing graphene (or) graphene derivatives causes large coloumbic forces occurring due to same polarities. So we added additional compound named chitosan which has opposite polarity to overcome this force. Chitosan is a non-toxic substance and has natural ability to cling to the surface with good mechanical strength [20]. Chitosan also has the ability to improve enzyme absorption so it is very suitable for our measurement. Therefore, we achieved higher performance by adding chitosan on high conductivity graphene and then lastly the DNA was comfortably added to the surface [4].

The recent study has indicated that graphene-chitosan device showed higher electron transfer rate when compared to device based on graphene oxide. Thus, we can conclude from the results that suitable microenvironment can be obtained at the surface by using graphene [4].Similar results has been observed from a study by using chitosan which indicated that molecules can be immobilized onto the surface by using chitosan on the top of graphene which further improved the performance by using the chemicals for impedance sensing [15]. Therefore by using this model we achieved higher sensitivity and selectivity from our measurement results at high frequency.

1.5 Low Loss conductors for RF applications:

In this section we try demonstrate the integrated on-chip inductors which has quality factor by using the low loss artificial conductor material which is based on ARLYM superlattice. Low loss conductors are used in electronics to overcome the drawback of passive components on the circuit and also to improve the RC delay which is mainly caused due to the interconnects.

In our method we make use of the artificial meta-material which consists of several layers of $Ni_{80}Fe_{20}$ and copper which are arranged on top of each other [2, 35]. Therefore, by monitoring the thickness of each layer the skin effect can be minimized to large extent [35]. We use the high saturation magnetic material named FeCo to tune to lower frequencies [2]. Due to a very large increase in the density of the devices the performance can be greatly affected due to the lower size. On the other hand we also have the complexity which arises due to wiring between the interconnects. Later we observe that there is a greater propagation delay as the device dimensions decrease further to about 0.18 um which leads to noise and increase in the power dissipated. Therefore all the above are the major issues noticed and become the limiting factor in large scale integrated circuits [7].

Previously the cost of the system was high as the devices occupied large area therefore, we added high permeability film to the fabrication to overcome this effect. This methodology is proven to be very effective and can be easily integrated with the existing Si technology. But the major drawback of the above method is it resulted in poor quality factor, eddy current loss, low ferromagnetic resonant frequency (FMR) etc.

The interconnect delay caused also reduces the speed of the signal and energy dissipation. The switching delay also grows and becomes larger. Therefore, these effects become worse when we reach to 35 nm technology.

In high performance microprocessors we suffer the interconnect delay and losses so we make use of synchronous clock to reduce these effects and also rise the clock frequency. But these effects are more prominent at higher frequencies and especially when we integrate some passive devices. Therefore, in order to reduce all the above effects and minimize interconnect RC delay

we use conductors with improved conductivity value. Among all the conductors available copper is widely used conductor due to its high conductivity at room temperature. At high frequencies we consider the ohmic loss in conductors due to low conductivity value (σ) and skin effect. Therefore, it is very important to minimize the skin effect in order to decrease the RC delay and metal losses.

Skin effect :- "Skin effect is defined as the ability of the electric current to flow near the surface of the conductor within the surface depth at high frequency" [29].

$$\delta = \sqrt{1/\pi f \sigma \mu_0} \qquad (1.5.1)\ [29]$$

In eq-1.5.1 'f' is the frequency and μ_0 is permeability of vaccum [29].

From equation- 4.1.1 we observe that the skin depth is inversely proportional to frequency 'f' i.e, it decreases with increase in frequency. Therefore we can reduce the ohmic loss by operating at high frequency and by decreasing the effective cross-section of the conductor [35]. If we increase the thickness of conductor above certain skin depths to minimize the ohmic losses then we cannot reduce the metal loss [2].Thus, in order to improve the performance at high frequency operation we need to increase the skin depth. In our approach we try to increase the skin depth by bringing the effective permeability of the conductor to approximately zero. Hence, by doing so current can flow across the entire cross-section of conductor uniformly [2, 35].

The concept of effective permeability value of the conductor going close to zero is observed in magnetic films operating at anti-resonance frequency.

$$f_{AR} = (\gamma / 2\pi)(M_S + H_0) \qquad (1.5.2)$$

In equation-1.5.2 "γ is known as the 'gyromagnetic ratio', 'M_s' is 'magnetic saturation' and 'H_0' is the 'anisotropy' of the magnetic field" [42, 39, 45].

Inspite of having the permeability value close to zero the magnetic materials have very low conductivity so they cannot be used as low loss conductors. Therefore, we came up with the new concept of combining the metal with good conductivity and magnetic films together with anti resonant behavior in order to overcome the problem of low conductivity of magnetic materials. Recently an artificial layered meta-material called ARLYM has been developed for this purpose. Therefore, by making use of the above concept of artificial layered material skin effect can be suppressed effectively over a wide range of frequency.

In our approach we combined both copper and perm alloy ($Ni_{80}Fe_{20}$) layers at high frequency and skin effect suppression observed is compared to the copper (Cu) with high conductivity at low frequency [2]. This concept developed in our approach is fully compatible to the existing CMOS technology and can be easily adopted by the semiconductor industry [35]. The devices like inductors, transmission lines, waveguides etc, can be built based on this technology to obtain better performance at high frequencies [2, 35].

Thesis Outline:-

Chapter 1: Introduction: This gives an outline of classification of bio-sensors based on label based and label free approaches (section 1.1), Surface plasmonic resonance (SPR), Nanomaterials used for sensing and advantages of using nanomaterials for sensing application (section 1.2), CNTs (section 1.3), Graphene (section 1.4),Use of low loss conductors for RF applications (Section 1.5).

Chapter 2: Measurement Setup, S-parameters, De-embedding: This Chapter lays emphasis on measurement set-up (Section-2.1), Calibration introduction (section 2.2), Needs for system calibration (Section 2.3), 12 error-term model (section 2.4), SOLT calibration (Section-2.5), finally, the de-embedding (thru) procedure (Section-2.6).

Chapter 3: Bio-Impedance sensing mechanism, CPWs Design Experimental and simulation results: This chapter describes the methods used for bio-sensing (section 3.1), Bio-Impedance sensing mechanisms(section 3.2), Experimental procedure and AFM results (Section 3.3), Design of CPWs (Section 3.4), Measurement procedure (section 3.5), Impedance characterization (section 3.6), Simulation procedure and results (section 3.6),Extraction of substrate permittivity (section 3.7),Equivalent circuit model (section-3.9).

Chapter-4: "High quality factor RF inductors using low loss conductor featured with skin effect suppression for Standard CMOS/BiCMOS" [2, 35]: This chapter starts with the introduction of using low loss conductors (section 4.1), Structural parameters and experiments (section 4.2), Results (Section 4.3).

CHAPTER-2: Measurement set-up, S-Parameters & De-embedding procedure.

This Chapter lays emphasis on measurement set-up (Section-2.1), extraction of physical parameters like Propagation constant (γ), characteristic impedance (Z_0), etc, from measurement (S-Parameters) and explains the need for system calibration using the standard structures (Section-2.2) followed by de-embedding (thru) procedure (Section-2.6) in detail.

2.1: Measurement set-up:

Impedance measurements are performed on Cascade (M150) wafer probe station by registering 1-port S-Parameters by using Agilent network analyzer (PNA-N5230A) operating at frequency between 10 MHz-40 GHz. Network analyzer was used for measuring the scattering parameters upto 26 GHz (limited by the cable), which is connected to the PNA and the micro-probes as shown (Fig 2.1).

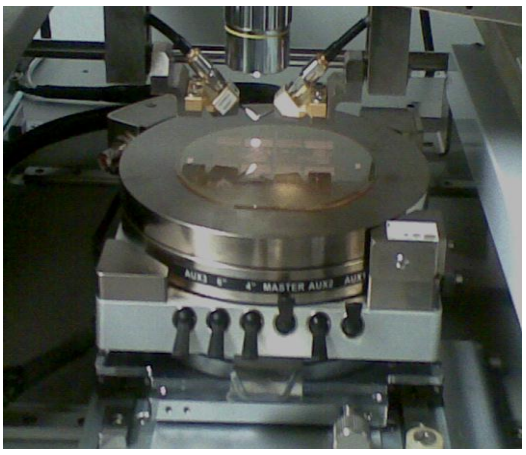

Figure 2.1: Measurement set-up

Cascade ACP-40 GSG (100) probes were used for performing the 'ground-signal-ground' measurement. G-S-G probes have been while performing our measurement as they are

electrically better when compared to the Ground-Signal (GS) or Signal-Ground (SG) configuration. The reason behind this is the field lines are coupled to the substrate on both sides of the signal line in G-S and S-G configuration as shown below (fig-2.2).

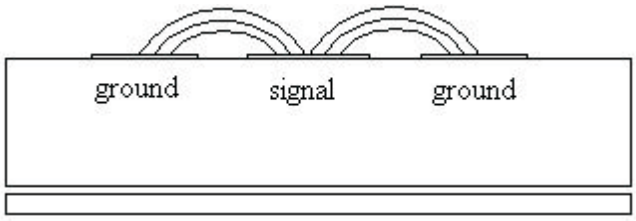

Figure 2.2: The fieldlines terminated on the ground lines

The amount of coupling depends on the substrate thickness and on the pad spacing. The probes must be kept clean. Dirt on the probes, like dust and metal parts, can influence the measurements due to extra parasitic effects.

In order to align the probes, a contact wafer is used to ensure a good contact from all the tips of the probes on the contact substrate. Before starting the experiments we need to make sure that the probes are in good contact with the bond pads, by looking at the amount of skate that is produced when placing the probes and verify on the VNA if a good contact is made. The full 2-port measurements were performed on all the devices on the wafer.

2.2: Calibration:

The system has been calibrated manually prior to the measurements in order to eliminate un-certainties in the measurement results. For this purpose a full 2-port open-short-load-thru (SOLT) calibration was carried out and this can also be verified mathematically by using the mathematical 12 error- term model.

2.2.1 Needs for system Calibration: In order to achieve accurate and reliable measurements, considering solely the effects of the DUT, calibration needs to be performed which is then followed by the de-embedding method. After calibration the results can be verified on smith-chart of the network analyzer.

The error correction method has been employed for system calibration. In general, the various techniques used to solve for the VNA error terms require measurement of calibration standards. The raw measurements obtained from the calibration standards are compared to the theoretical results. The differences between the expected and observed measurements are used to determine the error terms. Therefore we used the open-short-load-thru (SOLT) calibration method in our approach. In this method calibration of each individual standard such as open, short, load and thru (fig-2.4(a)) has been performed and compared to the theoretical result. We can verify the calibration by interpreting the result on the smith chart of the network analyzer and also by observing the magnitude plot (dB) [9]. We need to verify the calibration of each standard on the substrate to ensure that the measurement results obtained are consistent and as expected. After performing the calibration the measurement can be performed. Therefore, by following this method we can achieve reliability in the measurement results.

We can also calculate the errors due to the calibration of 2-port measurements mathematically by using the 12 error-term model as shown in section-2.2.2 to obtain better accuracy and reliability in the measurement data. Lastly we perform the de-embedding to remove the parasitic effects caused due to bond pads and interconnects between the pads and DUT which still exists even after the calibration.

2.2.2: Method of 12 error-term system calibration:

The 12-term error model is used to calculate the systematic error terms mathematically associated with the 2-port measurements. This model basically makes use of two individual models one for obtaining the forward error terms and the other for reverse error terms associated with the network analyzer while performing the 2-port measurements as shown in fig-2.3(a) and 2.3 (b). Each model calculates six forward error terms associated with the forward model and reverse error terms associated with the reverse model. Once these error terms are detected and calculated then we can further eliminate them easily to obtain accurate measurement results. Thus, this model is proven to be very useful for calculating the errors mathematically associated with 2-Port measurements.

The errors related to the model and signal leakage are mainly directivity and crosstalk errors. The directivity error is occurred due to the length of the cables and uncertainty between the measurement ports [5].The other errors relating to the reflection and transmission tracking are caused by the signal reflected from the ports. The directivity error causes the limitation in the dynamic range for reflection measurements and cross talk error causes limitation in transmission measurement. The source and load mismatch errors are related to the signal reflections. Source mismatch error is caused due to interaction between input and source match in the DUT. Similarly load mismatch error is caused in between the load and output of the DUT. The other errors such as reflection and transmission tracking errors are due to the frequency responses and imperfections at the receiver [26].

Therefore, we draw the signal flow graph of each model and apply mason's rule to calculate the error terms individually. Mason's rule is applied to the signal flow graph (SFG) is used to calculate the relationship between each individual node. Thus, the equations obtained from applying the masons rule are solved to calculate each individual error term.

Forward model:-

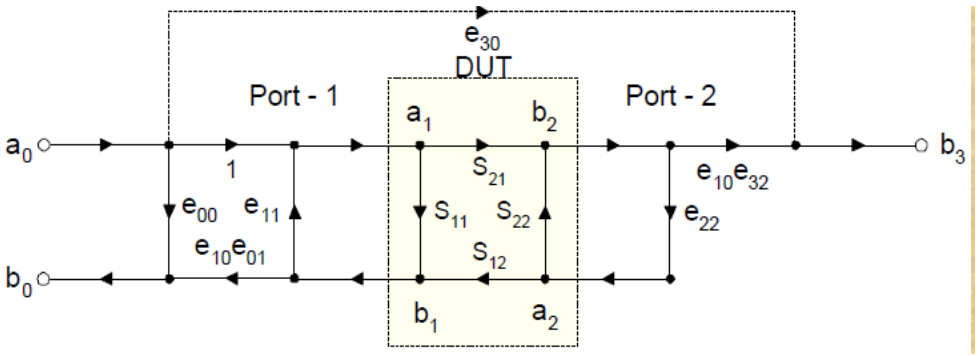

Fig-2.3(a): 12-term error model: Forward-model (Signal Flow Graph) [5].

In the above fig-2.3(a) we observe that there are 6-forward error terms associated with the signal flow graph as follows:

e_{00} = "Directivity error"

e_{11} = "error caused by Port-1 Match"

$e_{10}e_{01}$ = "Reflection tracking error"

$e_{10}e_{32}$ = "Transmission tracking error"

e_{22} = "error caused by port-2 Match"

e_{30} = "Leakage error"

To obtain the relation between any two nodes in the signal flow graph (SFG) we applied the mason's rule (stated below) given by equation 2.3.1:

$$T = \frac{[P_1[1 - \sum L_{(1)}{}^{(1)} + \sum L_{(2)}{}^{(1)}..] + P_2[1 - \sum L_{(1)}{}^{(2)} + \sum L_{(2)}{}^{(2)}....]]}{1 - \sum L_{(1)} + \sum L_{(2)}} \qquad (2.3.1)$$

In the above equation-2.3.1 'P_1' and 'P_2' are the different paths connecting the variables [33], $\sum L_{(1)}$, $\sum L_{(2)}$ represents the 1st and 2nd order loops respectively and $\sum L_{(1)}{}^{(P)}$ gives the sum of all first order loops not touching path 'P' etc.

Therefore, applying the masons rule (eq-2.3.1) to the forward model (SFG) we determine measurement S-parameters S_{11M} and$S_{21M.}$

Which also contains error terms and actual S-parameters (S_{11}, S_{21}).

At port-1, in the above SFG we see that S_{11M} gives the relation between incoming signal (a_0) and outgoing signal (b_0). Where, S_{11M} is the measurement S-parameter. Therefore we have,

$$S_{11M} = \begin{pmatrix} b_0 \\ a_0 \end{pmatrix}$$

Thus, by applying masons rule we try to solve the relation for the two nodes a_0 and b_0 which gives forward error terms as follows:-

We know that in fig-2.3(a) there are three paths P_1, P_2, P_3 in between a_0 and b_0 and they can be written as:

$$P_1 = e_{00},\ P_2 = S_{11}e_{10}e_{01},\ P_3 = S_{21}e_{22}S_{12}e_{10}e_{01};$$

The product of 1st order loops $\sum L_{(1)}$ is given by

$$\sum L_{(1)} = S_{11}e_{11} + S_{22}e_{22} + S_{21}e_{22}S_{12}e_{11}$$

Similarly, the product of 2nd order loop $\sum L_{(2)}$:

$$\sum L_{(2)} = S_{11}e_{11}S_{22}e_{22}$$

The product of First order loops not touching path-1 is given by:

$$\sum L_{(1)}{}^{(1)} = S_{11}e_{11} + S_{22}e_{22} + S_{21}e_{22}S_{12}e_{11}$$

Similarly, we get the product of first and second order loops not touching path-2 and path-3 as:

$$\sum L_{(1)}{}^{(2)} = S_{22}e_{22}$$

$$\sum L_{(2)}{}^{(2)} = 0$$

$$\sum L_{(1)}{}^{(3)} = 0$$

$$\sum L_{(2)}{}^{(3)} = 0$$

$$\sum L_{(2)}{}^{(1)} = S_{11}e_{11}S_{22}e_{22}$$

Finally, by plugging each term in equation for mason's rule we obtain the measurement S-parameter S_{11m} as shown:-

$$S_{11M} = \frac{b_0}{a_0} = e_{00} + (e_{10}e_{01})\frac{S_{11} - e_{22}\Delta_s}{1 - e_{11}S_{11} - e_{22}S_{22} + e_{11}e_{22}\Delta_s} \qquad (2.3.2)\ [5]$$

Similarly, using the same approach we can derive S_{21m} as follows, Where S_{21M} is measured S-parameter S_{21}.

$$S_{21M} = \frac{b_3}{a_0} = e_{30} + (e_{10}e_{32})\frac{S_{21}}{1 - e_{11}S_{11} - e_{22}S_{22} + e_{11}e_{22}\Delta_s} \qquad \text{(2.3.3) [5]}$$

Where, $\Delta_s = S_{11}S_{22} - S_{21}S_{12}$

Reverse error model:-

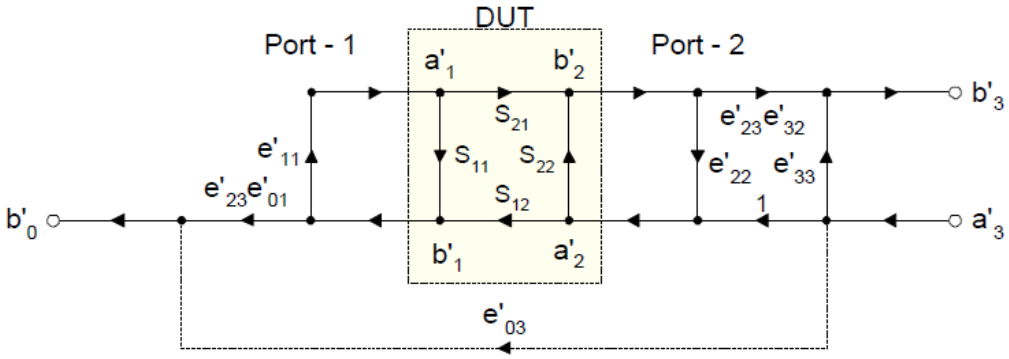

Fig-2.3(b): 12-term error model: Reverse model (Signal Flow Graph) [5]

The reverse error terms associated with the above drawn SFG are as follows:

e_{33}^{1} = Directivity

$e_{23}^{1}e_{01}^{1}$=Transmission Tracking

e_{11}^{1}=Port-1 Match

e_{22}^{1}=port-2 Match

$e_{23}^{1}e_{32}^{1}$=Reflection Tracking

$e_{03}{}^{1}$= Leakage

The measurement parameters for the reverse model (SFG) are also obtained by using the mason's rule and repeating the same procedure as we did for forward model. Therefore, we obtain the other two measurement parameters S_{22M} and S_{12M} as shown.

$$S_{22M} = \frac{b_3'}{a_3'} = e_{33}' + e_{23}' e_{32}' \frac{S_{22} - e_{11}'\Delta_s}{1 - e_{11}' S_{11} - e_{22}' S_{22} + e_{11}' e_{22}' \Delta_s} \quad (2.3.4)\ [5]$$

$$S_{12M} = \frac{b_0'}{a_3'} = e_{03}' + e_{23}' e_{01}' \frac{S_{12}}{1 - e_{11}' S_{11} - e_{22}' S_{22} + e_{11}' e_{22}' \Delta_s} \quad (2.3.5)\ [5]$$

Similarly, $\Delta_s = S_{11}S_{22} - S_{21}S_{12}$

We observe that the above equations for both forward and reverse models that it contains both actual S-parameters combined with the error terms. Thus, we see that there are a total of four equations combined from both the models which contains four actual S-parameters and twelve error terms in total [5].

We find a way to determine all the twelve error terms and actual device parameters by solving the four equations obtained from both the error models. Therefore, we follow a three step procedure applied to both forward and reverse model to extract the error terms as shown below:

Step 1: We calibrate port 1 using open, short and load to obtain e00, e10e01 and e11 which gives the error terms.

$S_{12} = S_{21} = 0$; for open, short, load

Step 2: To calculate the leakage current we match connect a load (Z_0) to port-1 which gives us the leakage current error term.

$$S_{12} = S_{21} = S_{11} = S_{22} = 0;$$

$$e_{22} = \frac{S_{11M} - e_{00}}{S_{11M} e_{11} - \Delta_e}$$

$$e_{10} e_{32} = (S_{21M} - e_{00})(1 - e_{11} e_{22})$$

Step 3: We connect port-1 and port-2 together for thru to determine the remaining errors.

$$S_{12} = S_{21} = 1;$$

$$S_{11} = S_{22} = 0$$

Therefore, we obtained all the error terms associated with both models as follows

Errors corresponding to forward model:

$$e_{00} = S_{11ML} \tag{2.3.6}$$

$$e_{11} = \left[\frac{S_{11MO} + S_{11MS} - 2S_{11ML}}{S_{11MO} - S_{11MS}} \right] \tag{2.3.7} [5]$$

$$e_{10}e_{01} = \left[\frac{2(S_{11ML} - S_{11MS})(S_{11MO} - S_{11ML})}{(S_{11MO} - S_{11MS})} \right] \quad (2.3.8)\ [5]$$

$$e_{10}e_{32} = \left[\frac{(S_{21M} - S_{21ML})[S_{11MO}{}^{2}\,(1 - S_{11M}) + 2(S_{11MO} - S_{11MS})(S_{11ML}(S_{11MO} - S_{11MS}) + S_{11MS}(S_{11ML} - S_{11MO}) + S_{11ML}(S_{11M} - S_{11ML}))]}{(S_{11MO} - S_{11MS})(S_{11M} + S_{11ML})(S_{11MO} + S_{11MS}) - 2S_{11MS}S_{11ML} - 2S_{11M}S_{11MO}} \right]$$

(2.3.9)[5]

$$e_{22} = \left[\frac{2(S_{11M} - S_{11ML})(S_{11MO} - S_{11MS})}{(S_{11M} + S_{11ML})(S_{11MO} + S_{11MS}) - 2S_{11M}S_{11ML} - 2S_{11M}S_{11MO}} \right] \quad (2.3.10)[5]$$

$$e_{30} = S_{21ML} \quad (2.3.11)\ [5]$$

Error's corresponding to the reverse model:

$$e_{33}{}' = S_{22ML} \quad (2.3.12)\ [5]$$

$$e_{11}{}' = \left[\frac{(S_{22M} - S_{22ML})(S_{22MS} - S_{22MO})}{-(S_{22MO} + S_{22MS})(S_{22ML} + S_{22M}) + 2S_{22M}S_{22MO} + 2S_{22ML}S_{22M}} \right] \quad (2.3.13)\ [5]$$

$$e_{23}{}'e_{01}{}' = \left[\frac{2(S_{12M} - S_{21ML})(S_{22MS} - S_{22ML})(S_{22MO} - S_{22ML})}{-(S_{22MO} + S_{22MS})(S_{22ML} + S_{22M}) + 2S_{22MS}S_{22MO} + 2S_{22M}S_{22MO} + 2S_{22ML}S_{22M}} \right] \quad (2.3.14)\ [5]$$

$$e_{22}{}' = \left[\frac{2S_{11ML} - S_{22MO} - S_{22MS}}{S_{11MS} - S_{11MO}} \right] \quad (2.3.15)[5]$$

$$e_{03}{}' = S_{12ML} \quad (2.3.16)\ [5]$$

$$e_{23}{}'e_{32}{}' = \left[\frac{2(S_{22ML} - S_{22MS})(S_{22ML} - S_{22MO})}{S_{22MO} - S_{11MS}} \right] \quad (2.3.17)$$

Where, S_{11MS} is S_{11M} (short), S_{11MO} is S_{11M} (open) and S_{11ML} is S_{11M} (load).

Thus, in the final step we plug all the error terms in the equations obtained in order to determine the device parameters [5].

$$S_{11} = \frac{\left(\frac{S_{11M} - e_{00}}{e_{10}e_{01}}\right)\left[1 + \left(\frac{S_{22M} - e_{33}'}{e_{23}'e_{32}'}\right)e_{22}'\right] - e_{22}\left(\frac{S_{21M} - e_{30}}{e_{10}e_{32}}\right)\left(\frac{S_{21M} - e_{03}'}{e_{23}'e_{01}'}\right)}{D} \tag{2.3.18}$$

$$S_{21} = \frac{\left(\frac{S_{21M} - e_{30}}{e_{10}e_{32}}\right)\left[1 + \left(\frac{S_{22M} - e_{33}'}{e_{23}'e_{32}'}\right)(e_{22}' - e_{22})\right]}{D} \tag{2.3.19}$$

$$S_{22} = \frac{\left(\frac{S_{22M} - e_{33}'}{e_{23}'e_{32}'}\right)\left[1 + \left(\frac{S_{11M} - e_{00}}{e_{10}e_{01}}\right)e_{11}\right] - e_{11}'\left(\frac{S_{21M} - e_{30}}{e_{10}e_{32}}\right)\left(\frac{S_{21M} - e_{03}'}{e_{23}'e_{01}'}\right)}{D} \tag{2.3.20}$$

$$S_{12} = \frac{\left(\frac{S_{12M} - e_{03}'}{e_{23}'e_{01}'}\right)\left[1 + \left(\frac{S_{11M} - e_{00}}{e_{10}e_{01}}\right)(e_{11} - e_{11}')\right]}{D} \tag{2.3.21}$$

Where,

$$D = \left[1 + \left(\frac{S_{11M} - e_{00}}{e_{10}e_{01}}\right)e11\right]\left[1 + \left(\frac{S_{22M} - e_{33}'}{e_{23}'e_{32}'}\right)e_{22}'\right] - \left(\frac{S_{21M} - e_{30}}{e_{10}e_{32}}\right)\left(\frac{S_{12M} - e_{03}'}{e_{23}'e_{01}'}\right)e_{22}e_{11}' \tag{2.3.22}$$

In our method, we obtained the actual parameters of the DUT by considering four independent measurements for Short, load, open and thru respectively.

While performing each individual measurement for open, short and load, we avoid any interference from port-2 (S_{12}=S_{21}=0) while calculating the error terms associated with port-1. Additionally we add a load Z_0 equals the characteristic impedance of the system (50Ω) for load measurement and we set (S_{11}=S_{22}=0) to calculate the leakage error term. The measurement for thru is done by combining both the ports together (S_{12}=S_{21}=1) thus, this gives all the remaining error terms. Therefore, the 12-term error model allowed us to calculate both the error terms and the actual DUT parameters mathematically and we can also relate this model to our practical measurements.

2.3: Short-Open-Load-Thru (SOLT):

We performed the SOLT calibration with four independent structures (SOLT) on the substrate to determine the 12-error terms in practical. In this method 4 individual electrical standards (open, short, load and thru) on substrate has been used in order to eliminate the parasitic effects shown in fig below.

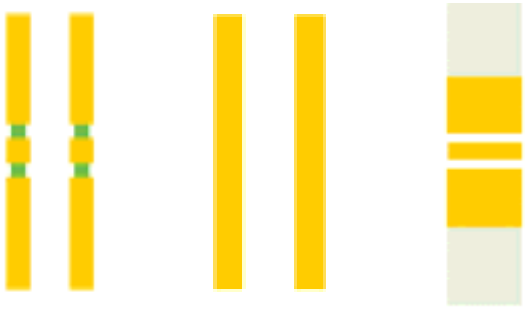

Fig-2.4(a): Short-open-load Standard structures:

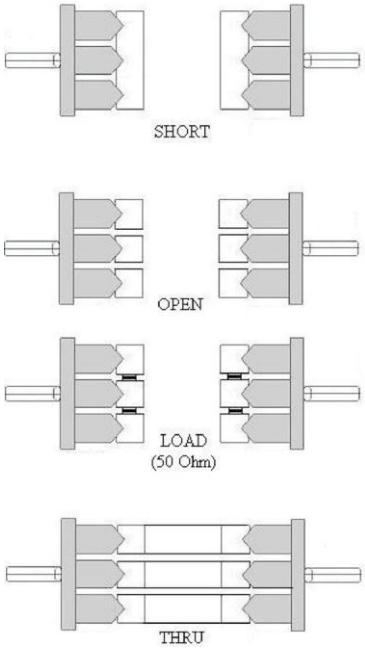

Fig-2.4(b): Short-open-load-Thru Standard after contact:

The calibration results obtained from each electrical standard has been observed on the network analyzer which gives sufficient accuracy over the mentioned frequency range.

SHORT: For a calibrating the short all GSG-probe pads are shorted. S-parameters has been recorded on the network analyzer by making a contact on the short structure placed on the substrate similar to that of load using probe as shown in figure- 2.4 (b). The two-ports are shorted in this case and S-parameters are set to $S_{12}=S_{21}=0$ as there is no interference in between the two ports. The result obtained from short has been verified on the smith chart which indicates that the result has to be concentrated towards the edge of the smith chart as shown (fig-2.4(c)) and then a magnitude of no more than ± 0.15 dB has to be obtained in order to verify the calibration for short. The short measures the parasitic inductance coming from the measurement equipment. In a Smith Chart the first measurement point for both *S*-parameters is found to be at 0

Ω. For a rising frequency sweep, the marker will always move counter clock-wise in a circular shape along the Smith Chart.

OPEN: The open calibration is performed by lifting the probe 200 μm above the substrate in order to avoid the parasitic effects caused by the other structures. Similarly the S-parameters has been calculated using the network analyzer. The results obtained indicate that a phase shift of 180 degrees from short has been observed as shown on the smith chart (fig-2.4 (c)).For an open calibration, the probes are placed on the pads. The open measures the parasitic capacitances of both ports. In the Smith Chart, the first measurement point starts at infinity (at the right end of the real axis).

LOAD: Load calibration is performed by making a contact using the probe on the load structure placed on the substrate shown below (fig-2.4(c)). Once the contact is made then this means the port is connected to the load which has impedance equal to the system characteristic impedance [24]. The system characteristic impedance is 50 ohm. Calibration result for the load has been recorded in the form of S-parameters on the network analyzer which is obtained by setting $S_{12}=S_{21}=0$ theoretically as we perform only 1-port measurement. The result of load calibration can be viewed on the smith chart and on the magnitude plot (dB) as shown below in order to verify the load characteristics. Thus, we observe from the results that the magnitude obtained is < 40 dB and the result on the smith chart must be focused towards the center. For the load, the probes have to be placed on a structure with two 100 Ω resistances in parallel, to minimize the inductance value.

THRU: For thru, the probe pads of the GSG probes are connected to each other in parallel by means of three lines. The most important S-parameters of this transmission standard are S_{21} and

S_{12}, respectively known as the forward and reverse transmission coefficients, or forward and reverse delay. After the calibration is performed the measurement results has been stored on the VNA. From the smith chart we observe that the impedance falls in the center of smith chart and will be close to approximately 50 Ω. The S-parameters for thru has been calculated by making contact on thru structure on the standard substrate. The S-parameters were calculated by using the network analyzer. For thru calibration the two ports are joined together which sets the S-parameters as follows $S_{12}=S_{21}=1$; $S_{11}=S_{22}=0$.Thus, the result obtained from thru calibration is shown below (fig-2.4 (c)):

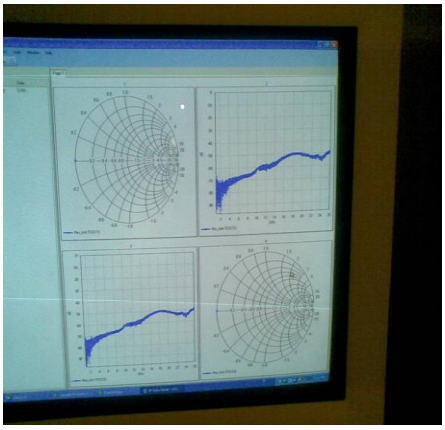

(a) Load

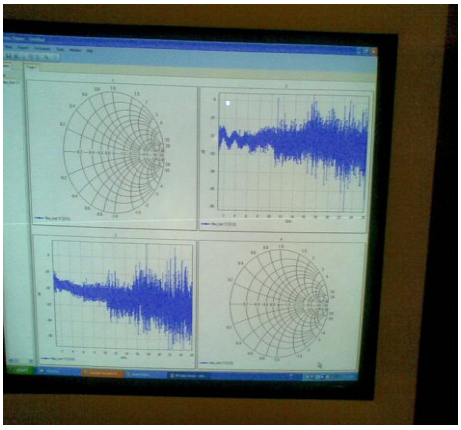

(b) short

In order to confirm the calibration we perform the measurement on SOLT, The results obtained from the calibration measurement has been presented on the smith chart below (fig-2.4 (c)).

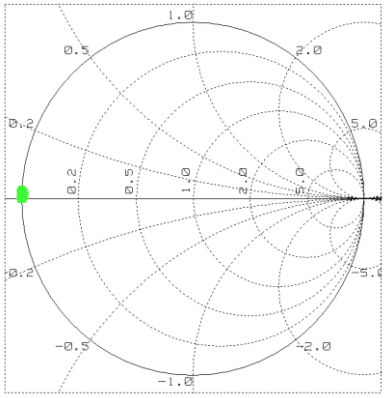

(a) Load

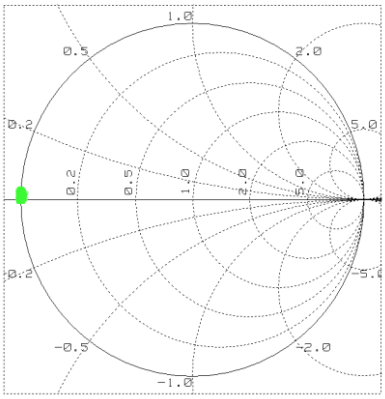

(b) short

.

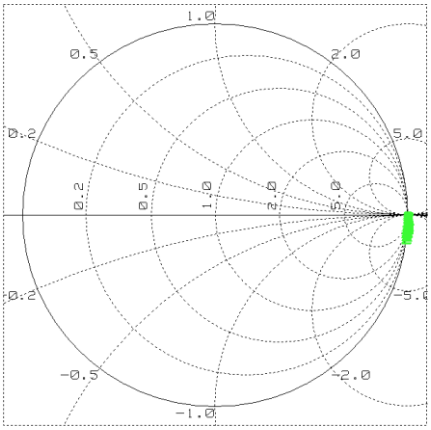

(c). thru

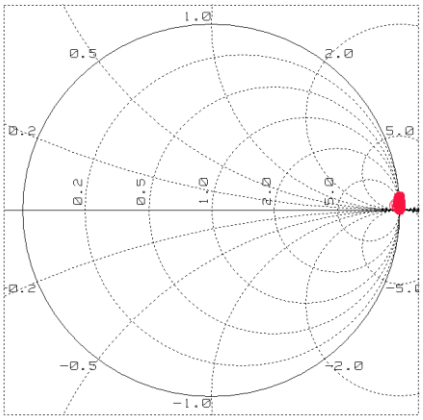

(d) open

Fig-2.4 (c): Open-load-short-thru (SOLT) Smith chart results

2.4 Scattering parameters:

At RF frequencies the Kirchhoff laws of currents and voltages are not applicable as the frequency is too high and as Kirchhoff laws does not take into account the influence of electrical and magnetic fields. The boundary condition states that the wavelength 'λ' must be much smaller than the size of the device. Therefore, while performing the two-port measurements difficulty arises and accuracy is lost by the influence of the probe and the bidirectional path of waves. The

use of scattering parameters or S-parameters offers the solution to this problem. The Scattering parameters can provide the gain, reflection and loss of the incident and reflected waves by recording the magnitude and phase.

The S-parameter matrix for a 2-port system is shown below:

$$S = \begin{bmatrix} S_{11} & S_{12} \\ S_{21} & S_{22} \end{bmatrix}$$

The above stated S-parameters are measured by using the vector network analyzer (VNA) and the results can be shown on the smith chart.

The figure below is the signal flow graph for a 2-port network:

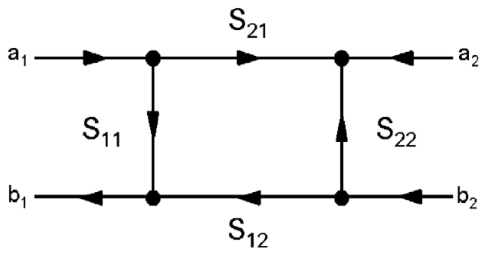

$$\begin{pmatrix} b1 \\ b2 \end{pmatrix} = \begin{pmatrix} s11 & s12 \\ s21 & s22 \end{pmatrix} \begin{pmatrix} a1 \\ a2 \end{pmatrix}$$

2.5 Thru De-embedding:

After the calibration is performed it is followed by de-embedding process. The most common de-embedding methods used are “open” and “short” method which uses the standard dummy structures [37]. There are several other advanced methods but they require high cost, larger area

and several patterns [17, 37]. Thus, we make use of thru-only de-embedding as it is simple to implement and requires measurement on only THRU structure.

De-embedding is used to remove the parasitic effects caused due to the bond pads and interconnects between the bond pads and the DUT. The parasitic effects tend to increase at microwave frequencies.

In this section we discuss the de-embedding method used in terms of design of the chosen de-embedding structure. The "open-short" de-embedding method is accurate at lower frequencies but at higher frequencies for RF measurements in order to avoid the complexity we consider the simple thru de-embedding structure. The "thru" de-embedding structure is required, because the contact resistance in between the probes and contact pads needs to be considered and also the contact pads on the test structures on-wafer uses different materials for different layers. The difference in the material gives extra contact resistance. The resistive and reactance losses between interconnects can be removed.

De-embedding is the process of deducing the actual device under test (DUT) characteristics from the measurements made at a distance. It is can be done on one or more dummy devices [17]. While performing the 2-port measurement we consider that the THRU pattern has reflection symmetry on both left and right sides. Therefore, by using this phenomenon we can split the THRU structure into two symmetrical halves called the error boxes. Then the scattering matrix for each individual box can be written separately. Once we know the scattering matrices for each box then we can easily eliminate the effects caused by the pads and leads in order to obtain the actual device parameters.

The de-embedding method discussed can also be applicable to higher frequencies for characterizing the on-chip transmission line. The results obtained from thru de-embedding are found to be consistent with the open-short de-embedding method. The parasitic elements caused by the measurement equipment, probes and losses introduced due to the cables will be removed during the calibration. The S-parameters obtained from calibration results on the VNA are automatically subtracted from the measurements when performing the measurement on de-embedding structures. The position of the reference plane will be altered by means of calibration. Thus, this is a boundary region which defines where the measured system will end. The quality of 2-port calibration is mainly determined by the load termination. After the calibration the reference plane will be at the probe tips and should be shifted from the probe tips to the device under test (DUT) by the means of de-embedding (Fig-2.6). Thus, the parasitic effects caused by the bond pads and interconnects can be removed by means of de-embedding.

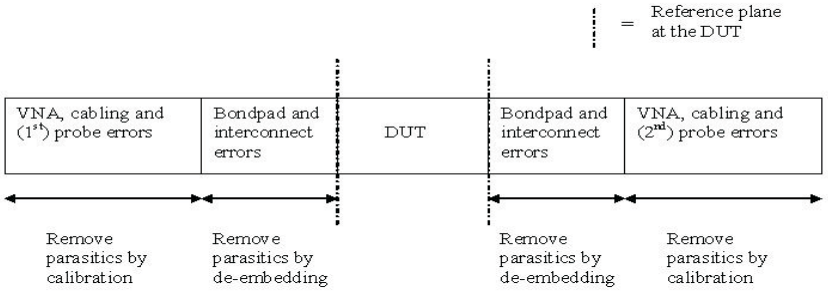

Figure 2.6 (a): The reference planes after calibration and de-embedding.

Thus, the method of thru de-embedding is proved to be accurate, reliable and very simple to implement by inserting a device under test (DUT) in between the error boxes. The error boxes are assumed to be symmetrical to each other. As this technique is simple and mathematical it is proven to be a preferred method when we deal with lumped elements at high frequencies [9].

We use the signal flow graph (SFG) to explain the "de-embedding" process mathematically shown in figure-2.6 (b) [9]. By applying the mason's rule we obtain the S-parameters for each individual error box and then subtract the result from the total obtained S-parameters in order to obtain the actual device parameters.

The procedure for thru-only de-embedding method is shown below:-

$$S_{Meas} = S_A S_{DUT} S_B$$

$$S_{Thru} = S_A S_B$$

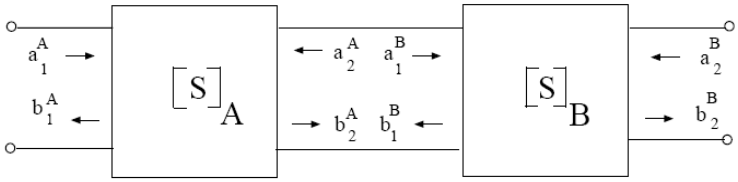

Figure 2.6(b): Thru de-embedding:

From the fig (2.6 (b)): $a_2 = b_3$; $b_2 = a_3$

$$\begin{pmatrix} b_1 \\ b_2 \end{pmatrix} = \begin{pmatrix} S_{11}{}^A & S_{12}{}^A \\ S_{21}{}^A & S_{22}{}^A \end{pmatrix} \begin{pmatrix} a_1 \\ a_2 \end{pmatrix}$$

$$\begin{pmatrix} b_3 \\ b_4 \end{pmatrix} = \begin{pmatrix} S_{11}{}^B & S_{12}{}^B \\ S_{21}{}^B & S_{22}{}^B \end{pmatrix} \begin{pmatrix} a_1 \\ a_2 \end{pmatrix}$$

$$\begin{pmatrix} b_1 \\ b_4 \end{pmatrix} = \begin{pmatrix} S_{11} & S_{12} \\ S_{21} & S_{22} \end{pmatrix} \begin{pmatrix} a_1 \\ a_4 \end{pmatrix}$$

By solving the above matrices we get,

$$S_{11} = \left[\frac{S_{11}{}^{A} + S_{11}{}^{B}\Delta_A}{1 - S_{11}{}^{B} S_{22}{}^{A}} \right] \tag{2.6.1}$$

$$S_{21} = \left[\frac{S_{21}{}^{A} S_{21}{}^{B}}{1 - S_{11}{}^{B} S_{22}{}^{A}} \right] \tag{2.6.2}$$

$$S_{22} = \left[\frac{S_{22}{}^{B} + S_{22}{}^{B}\Delta_B}{1 - S_{11}{}^{B} S_{22}{}^{A}} \right] \tag{2.6.3}$$

$$S_{12} = \left[\frac{1 - S_{11}{}^{A^2}}{S_{11}{}^{A^2}} \right] \tag{2.6.4}$$

If we assume, $[S]_A$ and $[S]_B$ are symmetrical then we have $S_{11}{}^{A} = S_{22}{}^{A}, S_{12}{}^{A} = S_{21}{}^{A}, S_{11}{}^{B} = S_{22}{}^{B}$, $S_{12}{}^{B} = S_{21}{}^{B}$

And suppose $[S]_A$, $[S]_B$ are bi-sectional symmetrical to each other regarding $[S]_B$, and then port-1 is $\begin{pmatrix} b_4 \\ a_4 \end{pmatrix}$ while port-2 is $\begin{pmatrix} b_3 \\ a_3 \end{pmatrix}$ [34].

$$\begin{pmatrix} b_4 \\ b_3 \end{pmatrix} = \begin{pmatrix} S_{22}{}^{B} & S_{21}{}^{B} \\ S_{12}{}^{B} & S_{11}{}^{B} \end{pmatrix} \begin{pmatrix} a_4 \\ a_3 \end{pmatrix}$$

Then, we get $S_{12} = S_{21} = \left[\frac{S_{21}{}^{A^2}}{1 - S_{11}{}^{A^2}} \right]$ (2.6.5)

$$S_{22} = S_{11} = \left[\frac{S_{11}{}^{A} + S_{11}{}^{A}\Delta_A}{1 - S_{11}{}^{A^2}} \right] \tag{2.6.6}$$

CHAPTER-3: Bio-Impedance sensing mechanism, CPWs Design, Experimental and simulation results.

3.1 Introduction: This chapter focuses on the techniques used for bio-sensing, Design and structure of Co-planar waveguides (CPWs) using ADS, AFM measurement images, ADS simulation and experimental results obtained from the measurements, A method used for extracting the dielectric constant, conductivity and thickness of GO, Chitosan and DNA theoretically from the ADS simulation will be discussed.

3.2 Bio-impedance sensing mechanisms: The bio-impedance sensing mechanisms developed are used for elucidating two important terms named sensitivity and selectivity. The transduction mechanism is used for converting the recognizing event to a measurable signal [31]. For example, a single cell detection mechanism is used to understand how a certain cell will respond to certain changes in the environment and also to determine how the cell interacts with the neighboring cells [3]. The sensing mechanisms are broadly classified into two main categories such as: Label based and Label free techniques [3].

Bio-impedance sensing methods are simple and label free mechanisms with very low cost used for detection of bio-molecules [14]. On the other hand label based method depends on adding an additional label to the molecule. The major drawback of label based method is it provides high sensitivity but cannot offer good selectivity [3]. It is also very hard and complex to detect the changes which are occurred due to labeling [3]. In addition to the above labeling need more time and is expensive [14]. The real time measurements cannot be obtained with the label based method. Therefore, Label-free approach has been adopted in our method to avoid all the

complexities and changes occurring in the molecules by attaching the labels. Thus, both high sensitivity and selectivity has been achieved in our method [11].

The examples of some label free methods include surface Plasmon resonance (SPR), nano-cantilevers, nanopores etc [3]. The cantilever based method is used for detecting the DNA by measuring the change occurred in the bending or by observing the change in the resonant frequency as the molecules get bind to it. Above all stated methods surface Plasmon resonance (SPR) is widely used method for detecting the single binding in the molecules. SPR measures the change occurred as the surface binding is caused so we use this technique in our model [3].

Surface Plasmon Resonance (SPR):- SPR observes the binding between the molecules and detects the change occurred caused by the surface binding [3]. SPR method can be used to measure the interactions in the DNA, protein-ligand, antigen-antibody etc, Therefore, the SPR technique has been adopted in our approach as it exhibits distinct dielectric properties and ignores the ionic conductivity.

DC measurements have been performed previously at low frequencies which consider only the change occurring in resistance values (CNT) and excluded the information of reactance formed by the bio-/chemical-agent adsorption. In our method the RF/microwave impedance was measured of DNA attached on nano graphene oxide (GO) sheets. The single atomic layered graphene GO provides a large surface area, which improves the sensitivity. The RF impedance characterization was carried out up to 10 GHz on graphenen nano platelets attached with chitoson and DNA using a coplanar waveguides (CPWs) as the sensing platform. A remarkable change in the impedance was observed with this setup.

3.3: Experimental procedure and AFM results: A atomic layer of approximately 1.1nm thick graphene oxide (GO) was prepared by the chemical intercalation/oxidation approach and were verified by atomic force microscopy using Agilent-5420 SPM/AFM microscope.

Fig (3.1): Agilent SPM/AFM microscope

The graphene oxides were examined by putting a drop of the GO solution on a freshly cleaved mica substrate. With non-diluted solution the AFM image showed that graphene oxide coverage was thorough and complete (Fig 3.2). Gaps or holes were not observed in our experiments which indicate a sufficient surface coverage of graphene oxide, which is an important factor in understanding the electrical measurements. In order to measure the thickness of each individual GO sheet, we needed to dilute the solution (Fig 3.3) as the layers overlap in concentrated GO and it was difficult to measure thickness of each sheet. Therefore, the AFM result obtained from the diluted solution is as shown in (fig 3.3).

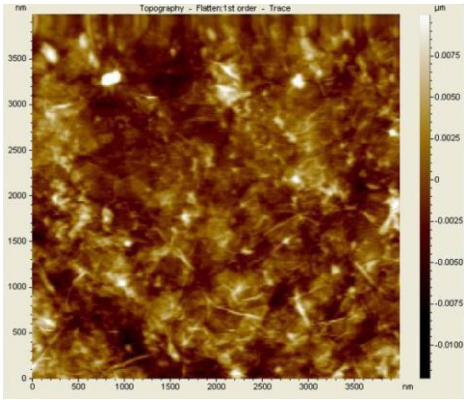

Fig (3.2): "AFM image of concentrated GO" [38].

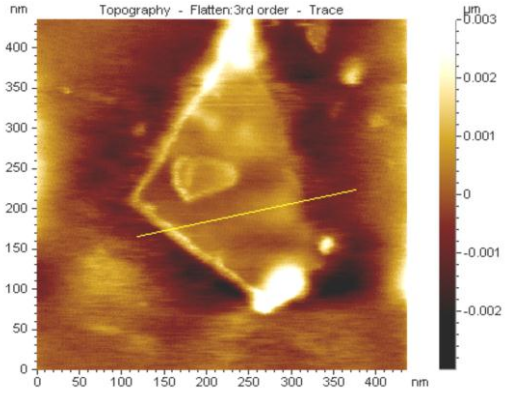

Fig (3.3): "AFM image of GO, diluted 1:100 ratio" [38].

The thickness distribution of the diluted GO obtained from a number of AFM measurements on different GO nano-platelets were plotted in order to get the average thickness (Fig 3.4).

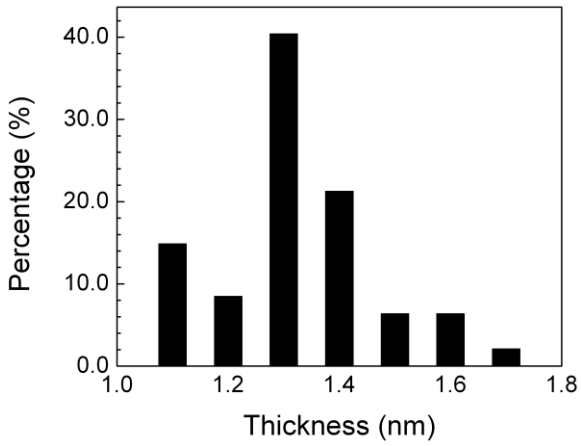

Fig (3.4): "Thickness distribution of the diluted GO" [38].

Statistically, the thickness of the graphene oxide obtained is around 1.3nm, roughly 3-4 atomic layers thick (Fig-3.4). The diluted sample showed graphene oxide nanosheets about 1nm thick in average; the concentrated sample showed overlapping of many layers of graphene, ensuring a complete surface coverage.

In order to take the full advantage of the frequency spectrum a number of CPWs were fabricated as a sensing platform (Fig 3.5). The single-sided planar configuration of the CPW opens access of attaching graphene and its derivatives. The target molecule will be attached at its surface. The configuration places the system being studied directly in contact with the CPWs, and effectively increases the sensitivity. Impedance measurements were performed on Cascade (M150) wafer probe station by registering single port S-parameters using Agilent network analyzer (PNA-N5230A), up to 26 GHz. Changes of impedance of the CPWs due to adsorption of target molecules can be noted in the form of scattering parameters (S-parameters). Thus, the presence of adsorption of molecules and surface interactions can be monitored.

3.4 Designing Co-planar waveguides (CPWs): A number of coplanar wave guides (CPWs) sensing platforms with various configurations, (Fig 3.5) were designed by using Agilent Advanced design system (ADS) and were fabricated on a glass substrate (AF-45) to eliminate the substrate loss [38].

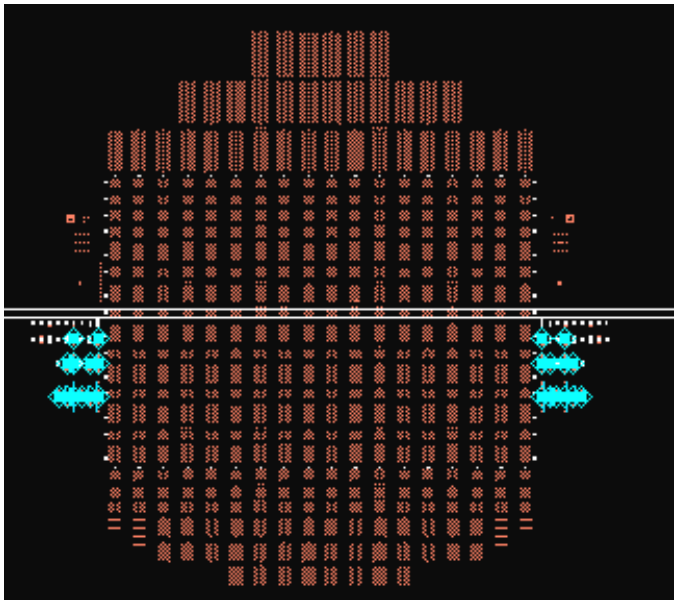

Fig (3.5): CPW design in ADS

Ti/Au was deposited in the fabrication of CPW. The 200 nm thick 'Ti' was used to improve the adhesion between the Au layer and the glass substrate. 'Au' was selected as the conductor because of its chemical inertness. Standard lift-off processing was employed to pattern the gold film into CPWs. The purpose of using glass substrate was to suppress the substrate loss at high frequencies. The CPWs were designed each with 50Ω characteristic impedance [38]. Meander type loads were fabricated with various impedances. The parameters of the three CPW devices used and the meander loads are listed (Table 3.1) [38]:

Device	L (μm)	W (μm)	S (μm)	Load(Ω)
A1	**1000.0**	**30.0**	**20.0**	**50.0**
B1	**1000.0**	**30.0**	**20.0**	**25.0**
C1	**1000.0**	**30.0**	**20.0**	**12.5**

Table: 3.1 [38]

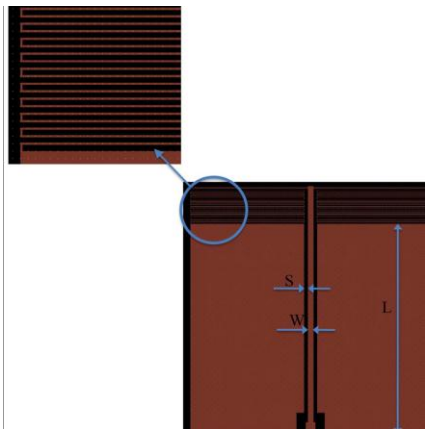

Fig (3.6): "CPW with meander load" [38].

Figure 3.6 shows the CPW line with meander load, where 'L' is the length of the signal line, 'W' is the width and 'S' is the spacing between the signal line and the grounds. The width of the meander lines is about 3μm, and the spacing between each meander line is 10 μm.

ADS simulation for S-parameters has been performed on all the devices by varying the spacing, width and also by varying the substrate values in order to match with experimental data obtained from the measurements. The conductivity values has also been changed starting from zero for reference measurement and varied in certain steps in order to extract the exact values of conductivity for GO, Chitosan and DNA. The result obtained from ADS simulation has been plotted separately for both real and imaginary parts using Origin (7.0) software. Thus, using this method the experimental and theoretical data results has been verified and discussed schematically (Section 3.7).

3.5 Measurement procedure: The reference measurements were performed on all the devices initially before dropping any chemicals on the wafer in order to study the effects on each individual device produced by dropping the chemicals in several steps. In the second step the device was coated with graphene oxide by putting a drop of approximately ~ 40 μl of graphene oxide solution onto the device such that the liquid connects and covers both lines. Sufficient coverage was ensured by putting the same amount onto freshly cleaved mica as that examined under atomic force microscope (Fig: 3.2). After drying and measurement, a drop of medium molecule weight Chitosan (Sigma-Aldrich) was placed on top of the graphene oxide coated area. This is because both the GO and DNA are negatively charged, a positive charge polymer (Chitosan) had to be used to adhere the DNA on the GO in order to avoid the repulsive forces acting on the similarly charged molecules. After drying, the device was connected to the PNA again for measurements. Since graphene oxide nanosheets are negatively charged, the positively charged chitosan will bind to graphene oxide through electric static interactions. Afterwards, a drop of calf thymus DNA (~1 μg/ml) was put on top of the polymer and measured after drying

under low-heat. Electrical properties of the device were measured on a PNA at a frequency range of 0.5-26.0 GHz.

3.6: Impedance Characterization: By, applying the concept of transmission line at RF/microwave frequency the load impedance Z_L can be written in terms of the input impedance Z_{in}, and wave propagation constant 'γ'(Equation 3.6.1).

$$Z_L = Z_0 \frac{Z_{in} - Z_0 Tanh(\gamma l)}{Z_0 - Z_{in} Tanh(\gamma l)} \qquad (3.6.1)[38]$$

Where, 'Z_0'and 'l' are the system characteristic impedance, and the length of the CPWs, respectively. The input impedance 'Z_{in}' (Equation 3.6.1) can be obtained from the measured one-port S-parameters S_{11} (Equation 3.6.2)

$$Z_{in} = \frac{1 + S_{11}}{1 - S_{11}} \qquad (3.6.2)\ [38]$$

Replacing (3.6.2) in equation (3.6.1), the load impedance can determined as shown (equation 3.6.3).

$$Z_L = Z_0 \frac{(1 + S_{11}) - Z_0 (1 - S_{11}) Tanh(\gamma l)}{Z_0 (1 - S_{11}) - (1 + S_{11}) Tanh(\gamma l)} \qquad (3.6.3)[38]$$

At low frequency, when $\Delta l << 1$, the load impedance can be determined directly from the S-parameters as shown (equation 3.6.4).

$$Z_L = \frac{1+S_{11}}{1-S_{11}} \qquad (3.6.4)[38]$$

Figure (3.7, 3.8) shows the resistance and reactance curves of measured load impedances as a function of frequencies. The three devices A1, B1, and C1 resonated at approximately 6.0 GHz, 10.5 GHz, and 20.8 GHz, respectively, manifested by reaching to the maximum of the resistance, and approaching to zero of the reactance. Since the lengths and the characteristic impedance of the devices were the same, we can conclude that the blue-shift of these resonant frequencies thus cannot be caused by the CPWs. On the other hand, the load consists of many turns of meander lines, (Figure 3.6). At high frequencies, these meander-shaped lines show significant values of inductance and capacitance, forming the LC resonances. More turns of the meander lines, means larger inductance and capacitance, and leads to lower resonant frequencies.

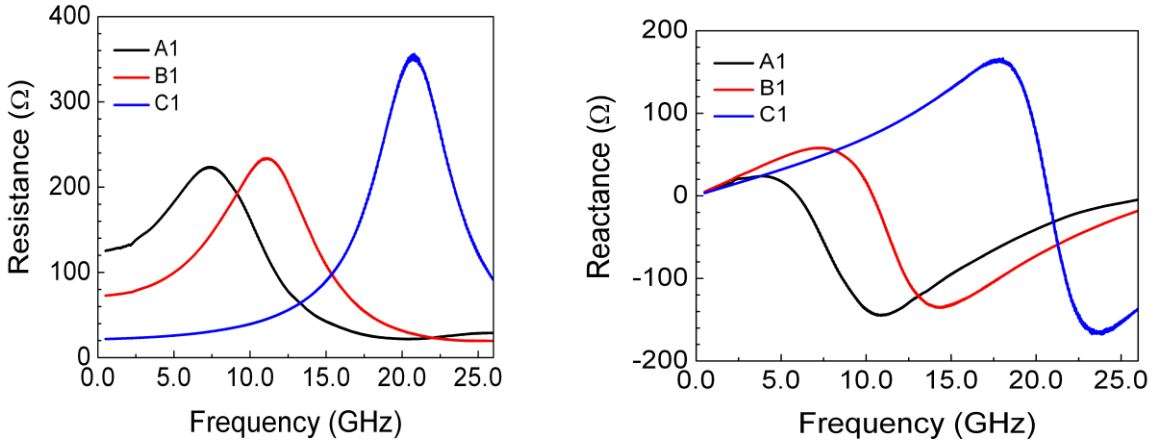

Fig: (3.7), (3.8): "Resistance& Reactance curves for devices A1, B1 & C1" [38]:

3.7 Simulation procedure and Results:

Advanced Design System ADS (Agilent) simulator was used for simulation. A number of Co-planar wave guides (CPWs) were designed with different configurations similar to the

measurement in order to verify the experimental results obtained .This was done by varying different parameters like spacing, width, dielectric constant, conductivity and the substrate values of CPW.

Only one device (C1) was considered for simulation as all the other devices designed has similar configuration and are symmetrical to each other except the number of turns on the load. Therefore we assume that if we can verify the simulation results on device C1 then the other devices also must show the similar effects and provide the same corresponding result. Moreover, device C1 had less number of turns on coil so this would save lot of simulation time.

Initially the simulation was performed for reference measurement on device C1 i.e. before adding any chemicals agents on the wafer. This was done by changing different dielectric constant (ε) values for the substrate. The ADS results obtained from simulation were in the form of S-parameters. We made use of Origin 7.0 for plotting resistance and reactance curves.

The dielectric constant value has been determined to be 4.05 which perfectly matched with the reference measurement for both resistance and reactance curves. The conductivity was used as zero as there were no additional chemicals attached to the substrate while performing the reference measurements. The simulation data obtained has been shown below (Figure 3.9) schematically for each measurement.

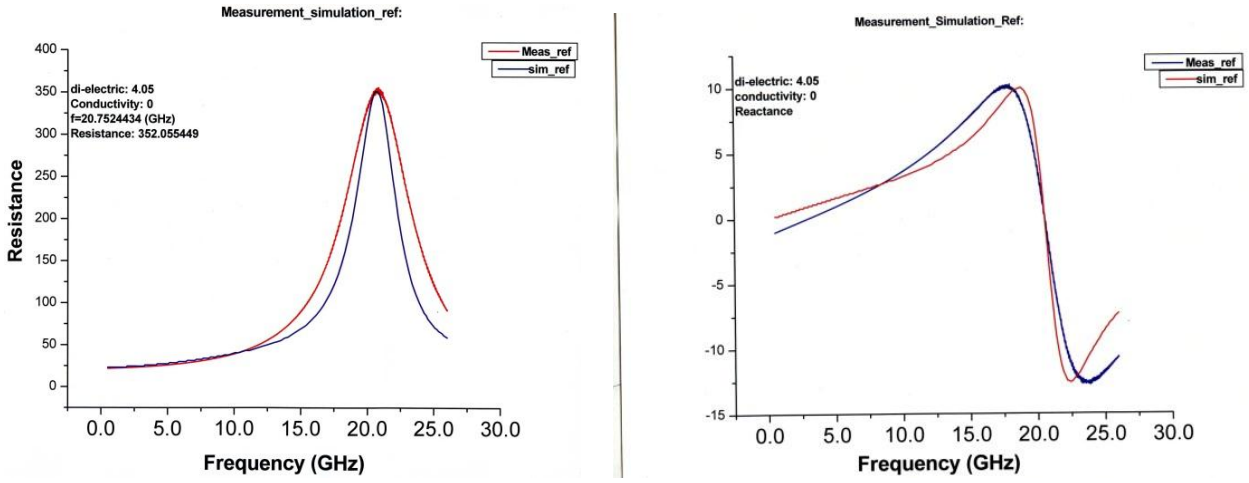

Fig3.9(a,b):Resistance & Reactance curves for reference simulation, dielectric constant(4.05), conductivity(0)

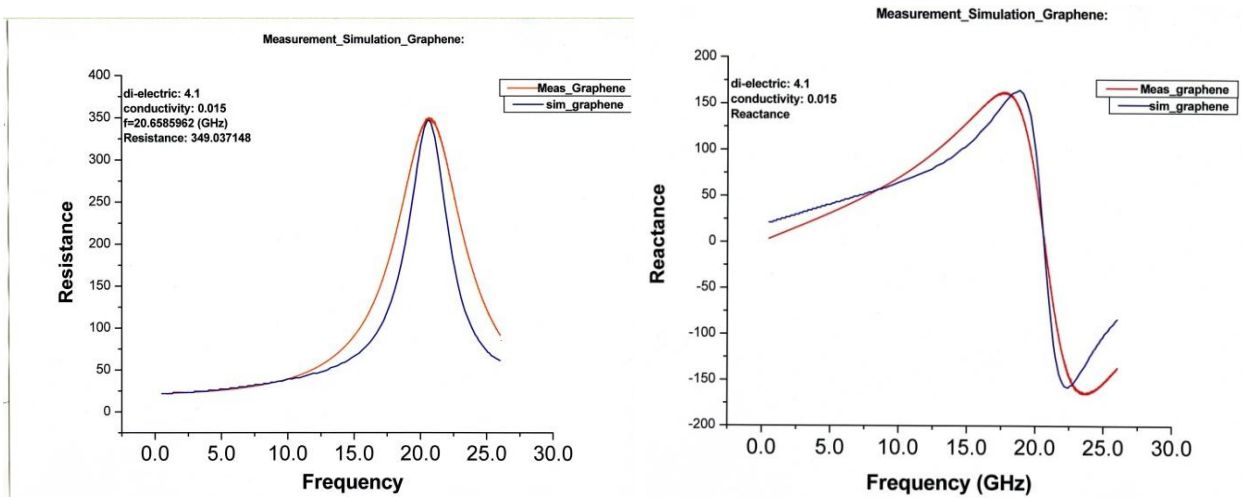

Fig3.9(c,d): Resistance&Reactance curves for graphene, dielectric constant(4.1), conductivity (0.015).

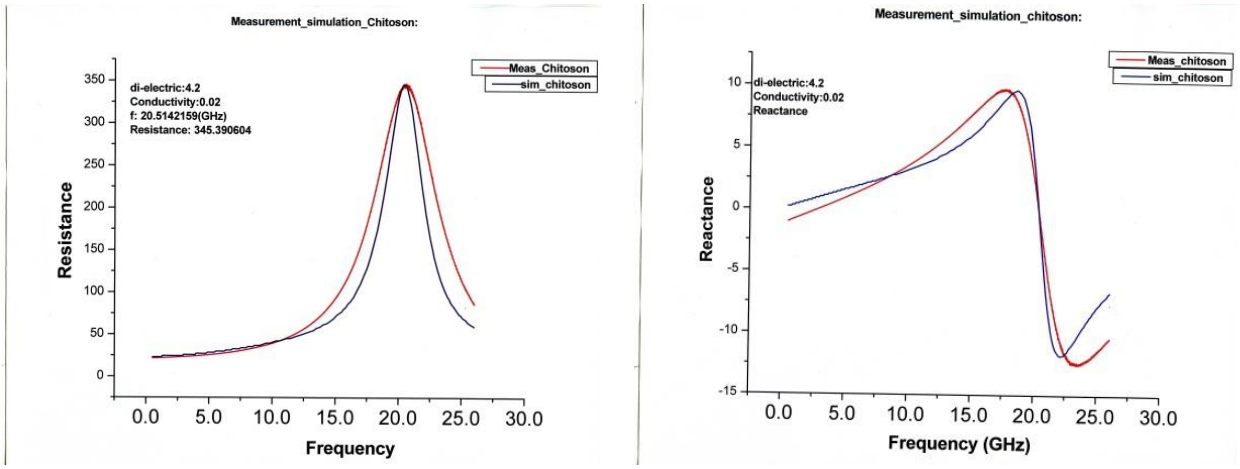

Fig3.9(e,f): Resistance&Reactance curves for Chitosan, dielectric constant(4.2), conductivity (0.02).

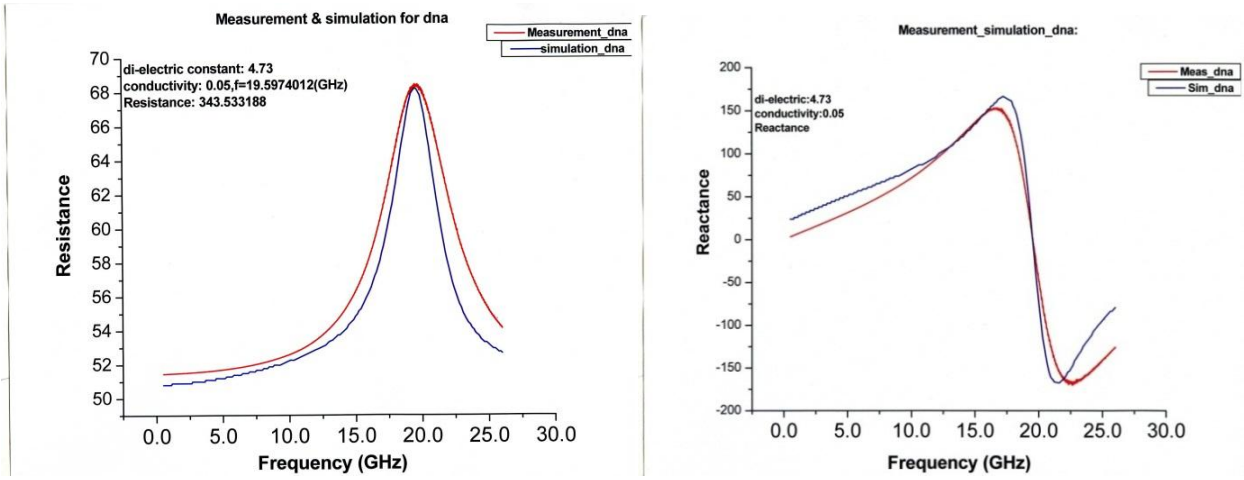

Fig3.9(g,h): Resistance&Reactance curves for DNA simulation, dielectric constant(4.2), conductivity (0.02).

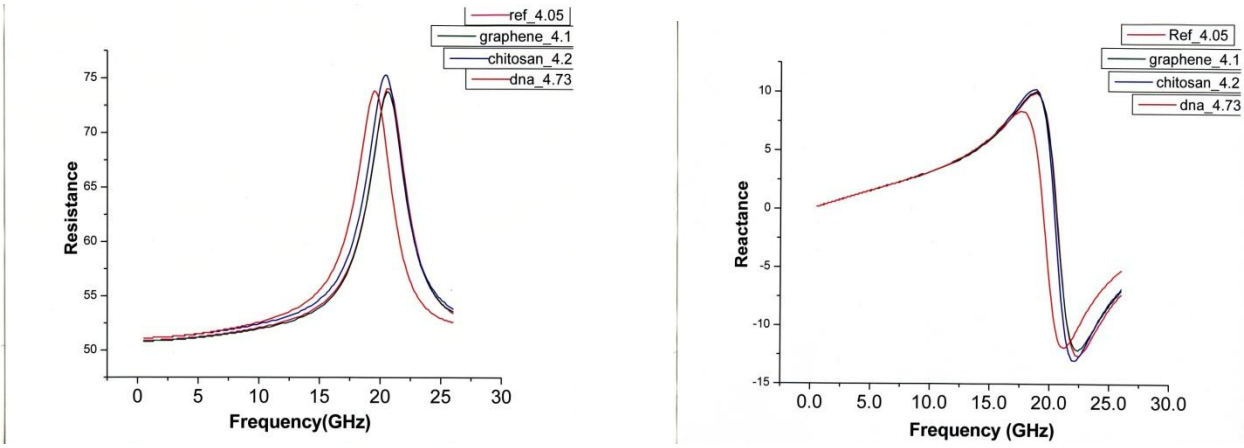

]

Fig3.9(I,J): Resistance&Reactance simulation curves for all layers showing shift in resistance towards right and match in reactance.

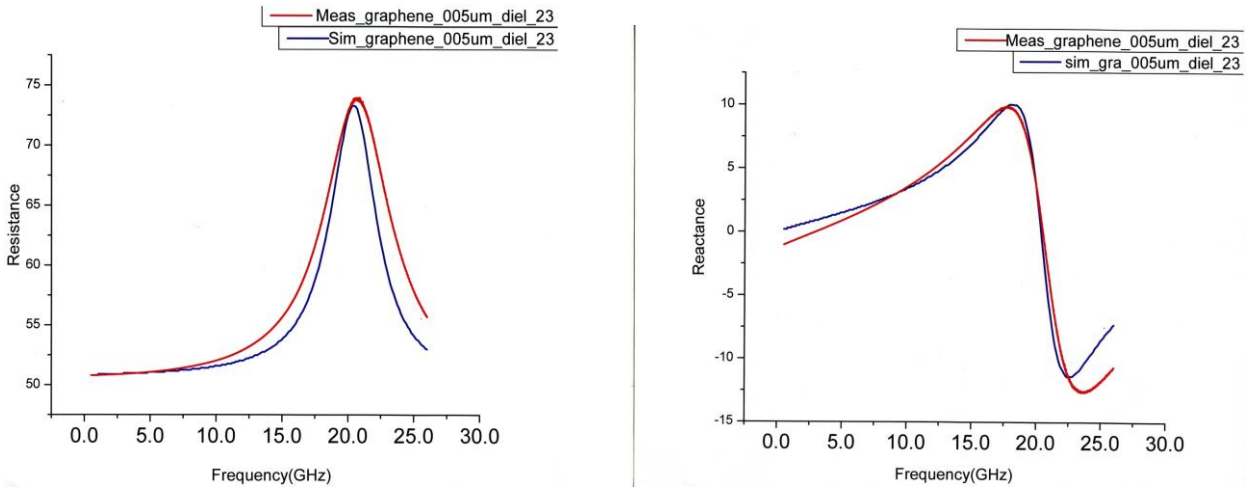

Fig3.9(K,L): Resistance&Reactance simulation curves for thickness of GO (0.05um).All the other parameters remains same.

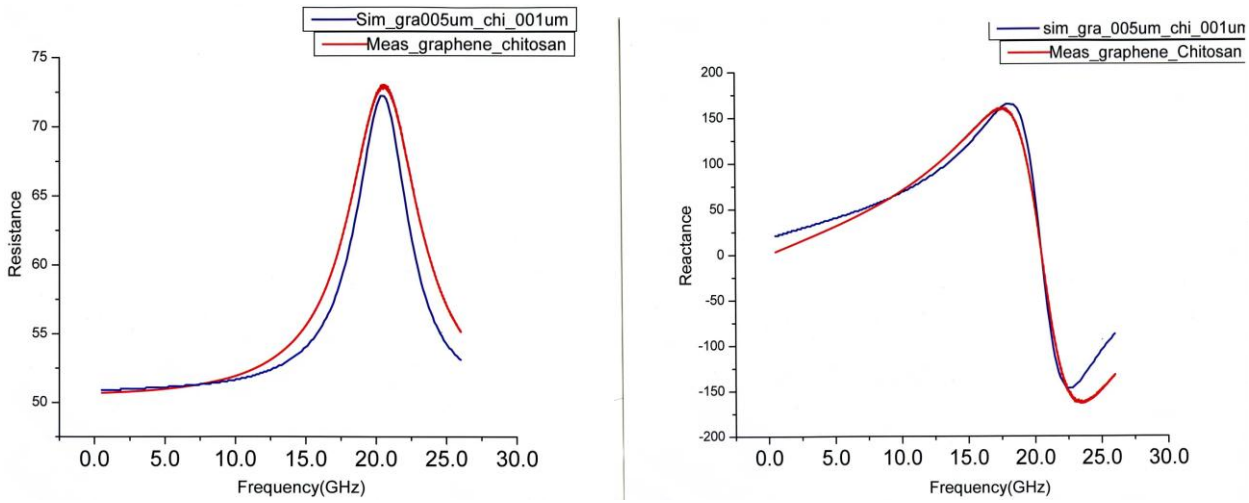

Fig3.9(M,N): Resistance&Reactance simulation curves for thickness of Chitosan (0.01um). All the other parameters remains same.

The next step we considered three models in order to add additional layers of chemicals like graphene, Chitosan and DNA while performing the simulation to extract different parameters.

For first model we added an additional graphene layer on the substrate but below the G-S-G interconnects. Then the dielectric constant of graphene was changed in steps by keeping fixed

the dielectric constant 'ε' for the substrate. This model was proved to be not very effective. As the effective permittivity value changes the capacitance also changes and thus, we observed shift in the opposite direction (right). Thus, we switched to the second model.

While considering the second model we considered the effective permittivity rather than adding any further layers on the substrate .The conductivity values were also changed simultaneously along with the effective permittivity in order to obtain the conductivity of graphene. The simulation curves resistance and reactance has been plotted for graphene as shown above. Therefore we obtained dielectric constant as 4.10 and conductivity as 0.015 for graphene. The similar approach was used for obtaining the dielectric constant and conductivity values of chitosan and DNA. The simulation results obtained for dielectric constant and conductivity has been listed (Table 3.2).Thus, this model was very effective for extracting both dielectric constant and their corresponding conductivity of the chemical agents. But we were not able to figure out the thickness of each layer using second model so we used the third model for extracting the thickness of each chemical added on the substrate.

The third model has been implemented for calculating the thickness of each layer added on the substrate by making use of the similar values obtained from the second model. For this model each layer is being added on the top above the (G-S-G) interconnects. By keeping the dielectric constant and conductivity values the same as obtained from second model we simply changed the thickness of the added layer and performed the simulation for different values of thickness. This method was repeated for all additional layers added and simulation was performed. The thickness of each layer obtained is listed in table 3.2 and the obtained resistance and reactance curves are shown above. Thus, all the parameters were determined and all the results from the simulation were verified with the experimental results.

3.8: Extraction of Substrate Effective Permittivity:

The results obtained from adding chemicals on the CPW devices were compared and presented. Significant blue shifts of *LC* resonant frequencies and decrease of resistance at these resonant frequencies were observed. By attaching various bio-/chemical- agents, due to the difference of the dielectric constants of agents, the parasitic capacitance of the meander loads were significantly modified. The change of the capacitance leads to the shift of the resonant frequency. Instead of three-dimensional electromagnetic simulation which requires long computing time, we performed two dimensional momentum simulation based ADS (Agilent). In the simulations, the change of the parasitic capacitance was counted as a perturbation to the substrate effective permittivity. Since the measurements were performed at RF/Microwave frequencies, both the real and imaginary part of the permittivity can be extracted, which is superior to the common DC resistance based sensing technology. The complex effective permittivity of the substrates was extracted from the momentum simulations using ADS (Agilent), and the results are listed (table 3.2). The non-zero conductivity indicated significant leakage currents in the graphene/graphene derivatives, Chitosan and DNA.

The below (Fig 3.9) shows the Impedance measurements results of the CPW device after each step of coating chemicals. The first shows the reference CPW measurement, the second shows the change observed when CPW was coated with graphene oxide; the third step represents the change observed when CPW was further coated with chitosan on the layer of graphene oxide and the fourth shows when DNA was further added on the CPW on layers of graphene oxide and chitosan.

At RF/Microwave frequencies, the dielectric constant is a complex quantity ($\varepsilon = \varepsilon' + j\varepsilon''$), consisting of a real part (ε') and an imaginary part (ε''). Since the dielectric constant of the GO is larger than air, adding GO increases the capacitance, and consequently decreases the resonant frequency. The change of capacitance is contributed by many terms, such as the real part of permittivity ε' , the remained thickness, packing density, and the surface coverage of the graphene oxide. Due to the complexity, it is impractical to determine the permittivity of the GO from the change in capacitance. On the other hand, the method of extraction of the substrate effective permittivity includes the non-uniform electrical field distribution in the substrate together with the fringe field in the air, regardless of the details of the film's structural information. Though it provides only the qualitative analysis, without losing generosity, the effective permittivity is still a good measure to sense the coated films. Since the results strongly depend on the structural properties of the remaining GO on the surface, the measurements on A1, B1, and C1 devices were done simultaneously sharing the same drop of GO. The same procedure is applied to the measurements after adding chitosan, and DNA. Similar blue-shifts of the frequency shift are observed by adding chitosan, and DNA. It is worth mentioning that (imaginary part of dielectric constant) ε'' is proportional to the conductivity (σ) of the film based on $\varepsilon'' = \frac{\sigma}{j\omega}$, where ' ω_0 ' is the angular frequency. The tangent loss is defined as $\tan\delta = \frac{\varepsilon''}{\varepsilon'}$. It turns out that, from the simulations, the presence of the leakage current leads to the decrease of the resistance at the resonant frequencies.

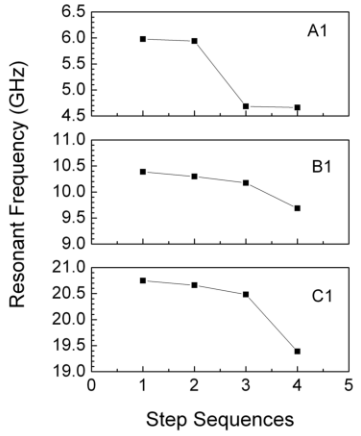

Fig (3.10): "Resonant frequency curves obtained for A1, B1& C1" [38]

Fig 3.10 shown below shows the shift in resistance at the resonance frequencies after each step coating. The first value indicates the result obtained from the reference CPW; the second shows the value when CPW was coated with graphene oxide; the third represents the value when the CPW was coated with graphene oxide and chitosan and the last result obtained shows the value when the CPW was coated with graphene oxide, chitosan and DNA.

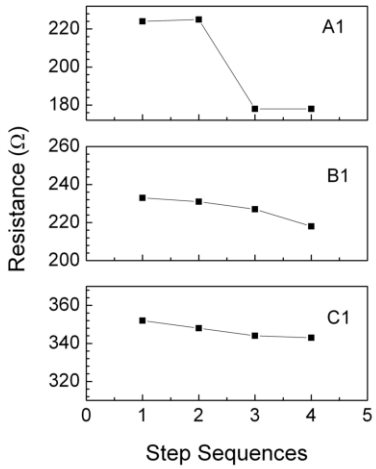

Fig: (3.11): "Resistance values plotted for devices A1, B1& C1" [38].

3.9: Equivalent circuit model: The equivalent circuit of load can be depicted by connecting resistors, an inductor (L) and a capacitor (C) in parallel. ' R_c 'is the resistance of the conductor,

and 'R_E' represents the leakage currents in the attached bio-/chemical- agents. The input impedance of the equivalent circuit without including the induced leakage current by the attached bio-/chemical-agents is shown (figure 3.11)

$$Z_{in} = R_{in} + jX_{in} \qquad (3.8.1)[38]$$

$$R_{in} = \frac{R_c(1-\omega^2 LC) + \omega^2 R_c LC}{(1-\omega^2 LC)^2 + \omega^2 R^2 C^2} \qquad (3.8.2)\ [3]$$

$$X_{in} = \frac{\omega L(1-\omega^2 LC) - \omega R^2 C}{(1-\omega^2 LC)^2 + \omega^2 R^2 C^2} \qquad (3.8.3)\ [38]$$

Where, 'R_{in}', 'X_{in}' and 'ω' are the real and imaginary part of the input impedance (Z_{in}), and angular frequency, respectively.

The resonant frequency (ω_0) is defined when X_{in} =0

$$\omega_0 = \sqrt{\frac{1}{LC} - \frac{R_c^2}{L^2}} \qquad (3.8.4)\ [38]$$

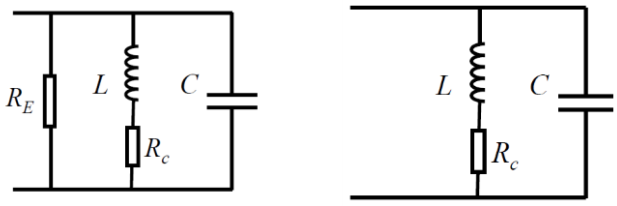

Fig (3.12) (a) & (b): "Equivalent circuit of CPW based sensor" [38]:

In the above model the resistance and inductance of meander load is proportional to the total length of the meander.If we consider the eddy current to be negligible then the resistance to inductance ratio will be constant.Therefore, the resonant frequency can be determined by the product of inductance ('L') and capacitance ('C').Now if we attach the chemical agent it leads

to increase in the capacitance therefore reducing the resonant frequency. The equation for resistance at the resonance frequency is given below (equation-3.8.5).

$$R_{in}(\omega_0) = \frac{1}{R_c} \tag{3.8.5}$$ [38]

Before attaching the bio-/chemical- agents, the input resistance at resonant frequency equals to the reciprocal of the resistance of the meander loads. This explains the observation of high resistance of device C1 at resonant frequency, due to its low load resistance (Fig. 3.7). After attaching bio-/chemical- agents, an effective resistance R_E representing the leakage current in the agents has to be considered (Fig. 3.11a). The shunt R_E will decrease the total resistance at the resonant frequency, which coincides with the measurements shown in (Fig. 3.10). Due to the presence of the leakage current, the total resistance was declined after adding the GO, chitosan, and DNA. The impacts of the leakage current of each coated bio-/chemical-agents are shown (table 3.2). The resonant frequency in the simulation result is determined by considering the relative value of the dielectric constant of chemical agents. However, the conductivity value also should be changed in order to match up to the resistance value at resonant frequencies. Thus, the quantitative analysis can depend on the film thickness and density.

	Step 1:	**Step 2: GO**	**Step 3: Chitosan**	**Step 4 DNA**
Dielectric constant (Relative)	**4.05**	**4.10**	**4.20**	**4.73**
tanδ	**0.00**	**0.015**	**0.02**	**0.05**
Thickness	**0.00**	**0.05um**	**0.01um**	

Table: 3.2 [38]

Thus, the results show that adding biomolecules to graphene oxide coated CPW sensors caused significant blue-shift in the resonance frequency and the decrease of the resistance onset of the resonant frequencies, reflecting the change of the complex permittivity of the attached biomolecules. Therefore, enabling of registering both the real and imaginary parts of the dielectric constant at RF/microwave frequencies show that this approach can be used to detect biomolecules.

Chapter-4: "High quality factor RF inductors using low loss conductor featured with skin effect suppression for Standard CMOS/BiCMOS". [4].

4.1 Introduction: This chapter demonstrates the integrated on-chip inductors with high quality factor by making use of a low loss artificial conductor which is based on "ARLYM" superlattice [39]. In this method we make use of the artificial layered material which consists of several layers of '$Ni_{80}Fe_{20}$/Cu' which are arranged on top of each other [42].We also considered the magnetic material such as FeCo and by adjusting the thickness of magnetic and non magnetic layers the skin effect has been minimized. By using this method we can tune to a frequency of 67 GHz and a high quality factor ~23 has been achieved at about 15 GHz [42].

Low loss conductors are being used in electronics to overcome the drawback of interconnect RC delay and also to improve the passive components. Earlier devices on-chip occupied large area and suffered from problems like low ferromagnetic resonant frequency (FMR), magnetic precision loss, eddy current loss etc. These effects were still observed even after introducing thin ferromagnetic film of $Ni_{80}Fe_{20.}$ On the other hand the RC delay in the circuit resulted in reduction of speed and dissipation of energy. Thus, these effects became more effective as we reached to 35 nm technology and the switching delay also became more than 100 times. In order to reduce the interconnect delay in microprocessors we used synchronous clock which also helps in the rise in clock frequency. But as we further move from gigahertz to terahertz microprocessors we see that the interconnect loss becomes even worse. Therefore, to overcome all the above problems we came up with the concept of using conductors with improved conductivity. By using the conductors with improved conductivity we can reduce the problem caused due to integrating

passive components in the circuit and RC delay. Copper is widely used conductor due to its high conductivity at room temperature.

At high frequency we see the skin effect and ohmic losses due the finite conductivity value. Therefore to reduce the RC delay and metal loss it becomes very important to decrease the skin effect.

Skin effect: - Skin can be defined as the ability of the electric current to flow close to the surface of conductor within the surface at certain depth at very high frequency. The equation for the skin depth is given as follows:

$$\delta = \sqrt{1/\pi f \sigma \mu_0} \qquad (4.1.1)\ [42]$$

In (eq-4.1.1) we know that 'f' is frequency and ' μ_0 'is permeability [39].

From eq-4.1.1 we observe that the skin depth is inversely proportional to frequency 'f'. The skin depth decreases as we operate at high frequency and this further will lead to increase in the ohmic loss [39].If we try to overcome the ohmic loss by increasing the thickness then we cannot see the decrease in metal loss [39]. So, in order to get high performance we have to increase the skin depth ' δ ' for high frequency.

We can increase the skin depth ' δ ' by reducing the permeability of the conductor (approximately to zero) which is observed in magnetic films at anti-resonance frequency. In this case we can observe that the electric current will be uniform across the conductor [42].

$$f_{AR} = (\gamma / 2\pi)(M_S + H_0) \qquad (4.1.2)\ [42]$$

In equation-4.1.2 "γ is known as the 'gyromagnetic ratio', 'M_S' is called 'magnetic saturation', and 'H_0' is 'anisotropy' of the magnetic field" [42, 39, 45].

Magnetic materials cannot be used as low loss conductors due to their low conductivity values. So we try to combine both metal and magnetic film to overcome this problem. Therefore, a conductor with high conductivity and magnetic film with anti-resonant behavior are combined in our approach. Recently the studies indicate that the artificial material named "ARLYM" has been introduced for this reason.

In our method we performed the experiments over a large range of frequency and compared the results to Cu reference. From the experimental data it is observed that the skin effect has been suppressed over the wide frequency when comparing to the conductor having high conductivity at low frequencies [39].

4.2 Structural parameters and Experiments:-The below figure (Fig-4.2.1) shows the structure of low loss conductors built with layers of $Ni_{80}Fe_{20}$/Cu.

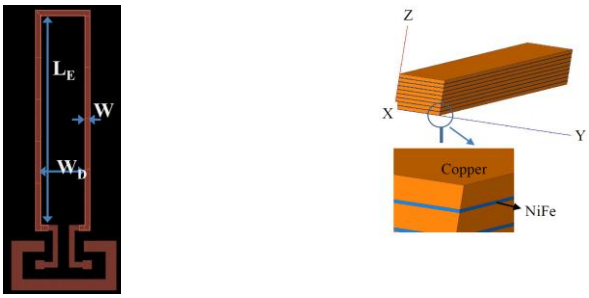

(a) (b)

Figure 4.2.1: "(a) Design of single turn spiral inductor with artificial layered metamaterial (ARLYM); (b) Sketch of the ARLYM consisting of a bi-layered $Ni_{80}Fe_{20}$/Cu superlattice with 8 periods on a glass substrate covered by a 10um buffer Benzocyclobutenes (BCB). ($t_{NiFe} = 50nm, t_{Cu} = 400nm$)" [42].

The thickness of $Ni_{80}Fe_{20}$ layer was about 50nm ($t_{NiFe} = 50nm$) and that of copper is 400nm approximately ($t_{Cue} = 400nm$) [40].The structure was built on glass (Schott AF45) in order to reduce the substrate loss and increase the effect caused by the conductor. The DC magnetron setting was used for depositing the layers using Trikon sigma. The deposition of layers was done at room temperature in the Argon ambient gas flow to avoid any oxidation on the surface. We used 8 inch target of each layer in order to get the uniform thickness. The uniformity obtained is about $\pm 2\%$ due to sputtering. The resistivity of Cu layer was about $1.83\ \mu\Omega$-cm and that of $Ni_{80}Fe_{20}$ is $16.3\ \mu\Omega$-cm [39].

In order to induce magneto crystalline anisotropy we used a magnetic field of approximately 10mT also used for obtaining thin film and uniform deposition [39].In order to reduce stress caused due to sputtering we made use of "Benzocyclobutenes" in between the layers [39]. The entire structure was then deposited on the glass substrate (AF45) [39]. The solution consisting of certain chemicals mixture with certain ratio (HNO_3: CH_3COOH: H_2SO4: H_20 = 2.5: 2.6: 1: 8.8) was used for wet chemical etching. The etching rate was about 300 nm/ min done at room temperature.

The table below (table 4.2.1) has listed the structural parameters of single turn spiral inductors which are made from NiFe (or) Cu multilayers.

	W_D (μm)	**L_E (μm)**	**W (μm)**	**Materials**
S22	**300**	**1200**	**20**	**NiFe/Cu**
S22-ref	**300**	**1200**	**20**	**Copper**

Table 4.2.1: "Structural parameters of single-turn spiral inductors" [39]:

For comparing we fabricated devices made of copper having thickness of 3.6 μm with the same configuration. The 2-port impedance measurements at a frequency of up to 26 GHz have been carried out by using wafer probe station. The S-parameters are obtained on the network analyzer (PNA N5230A).But prior to the measurements the system was calibrated using SOLT method and a single thru structure was used for de-embedding procedure. The de-embedding structure was used to extract the impedance of inductors.

4.3: Results obtained:-

4.3.1 Materials Characterization: Princeton AGM 2900 apparatus has been used for obtaining the magnetic hysteresis curves. The figure (Fig-4.3.1) is plotted for permeability versus the frequency for a single magnetic layer.

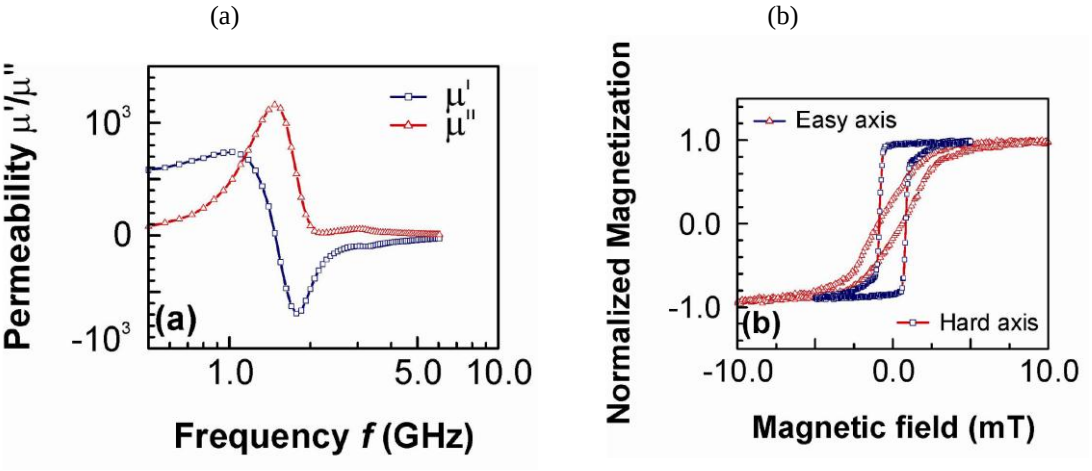

Figure 4.3.1: "(a) Extraction of frequency-dependent magnetic permeability of a NiFe film, (b) Magnetic B-H loop measurement of the NiFe film" [42].

A microstrip structure was fabricated for performing the electromagnetic simulation. The structure consisted of a $Ni_{80}Fe_{20}$ signal line on the top and ground at the bottom. The S-parameters were obtained based on the structure. The simulation was performed to extract the

permeability based on quasi-TEM mode. From the figure (Fig-4.3.1 (a)) we see that accuracy up to 6 GHz has been attained. The accuracy is obtained by using thin dielectric layers of SiO_2 of about 0.5 μm which separates the conductors. We also observe that accuracy is reduced as we go for higher frequency and as the real and imaginary part of permeability is close to zero. From the plot the real part of permeability becomes negative at frequencies above 1GHz.

4.3.2: Modeling of Magnetic permeability:

In a long conducting strip the magnetic field caused due to electric current is perpendicular to the direction of strip. In addition to the above we notice that far away from the lateral edge the induced field lies in plane of the stripe. The equation for effective permeability in a plane can be given by equation 4.3.2.1 where we assume that the thicknesses of each layer t_{NiFe} and t_{Cu} are less than the skin depth.

$$\mu_{eff} = \mu_0 \frac{\mu_\perp t_{NiFe} + t_{Cu}}{t_{NiFe} + t_{Cu}} \qquad (4.3.2.1)\ [42]$$

In the above equation 4.3.2.1 ' $\mu_\perp$ ' is the relative permeability.

The equation for in-plane permeability of ferromagnetic layer is given by the equation 4.3.2.2. We assume that the magnetization along the stripes is static.

$$\mu_\perp = \frac{f_{AR}^2 - f^2}{f_{FMR}^2 - f^2} \qquad (4.3.2.2)\ [42]$$

In equation 4.3.2.2 ' f_{FMR} ' is ferromagnetic resonance frequency which is given by the "Kittel" formula given by the equation 4.3.2.3

$$f_{FMR} = (\gamma / 2\pi)\sqrt{H_0(H_0 + M_S)}\,. \qquad (4.3.2.3)[42]$$

In practical ' $\mu_\perp$ ' is caused by the magnetic relaxation loss and it is complex. The ferromagnetic resonance frequency ' f_{FMR} ' can be considered by using equation 4.3.2.4 shown below.

$$H_0 \rightarrow H_0 + i(2\pi f / \gamma)\alpha \qquad (4.3.2.4)[42]$$

Where ' α ' is Gilbert damping constant.

The real part of the quantity ' $\mu_\perp$ ' which is given by $\mu_\perp = \mu'_\perp + i\mu''_\perp$ is negative for small value of ' α ' in the frequency range $f_{FMR} < f < f_{AR}$ as shown in the figure 4.3.1.But from the equation-4.3.2.1 the real part of effective permeability ' μ_{eff} 'disappears when $\mu'_\perp = -t_{Cu} / t_{NiFe}$. Thus, the above effect is similar to the ferromagnetic anti-resonance seen in single film and this frequency is known as effective anti-resonant frequency ' f_{EAR} '. The effective anti-resonant frequency depends on the properties of the magnetic layers like ' M_S 'and ' H_0 ' and also on the thickness ratio ' $r = t_{Cu} \diagup t_{NiFe}$ '.Thus, we assume that the skin depth can lead to uniform current distribution across the conductor [39].Therefore, all this discussion is based on the ferromagnetic superlattice.

In order to explain the distribution of current across the cross section of the conductor (ARLYM) clearly we performed the simulation and compared the result to the Cu reference. While performing the simulation we considered the thickness of NiFe to be 100nm and Cu as 400 nm to explain the skin effect suppression. The ARLYM superlattice consisted of 16 periods of NiFe or Cu layers. Thus, the similar effect should be observed with the inductors.

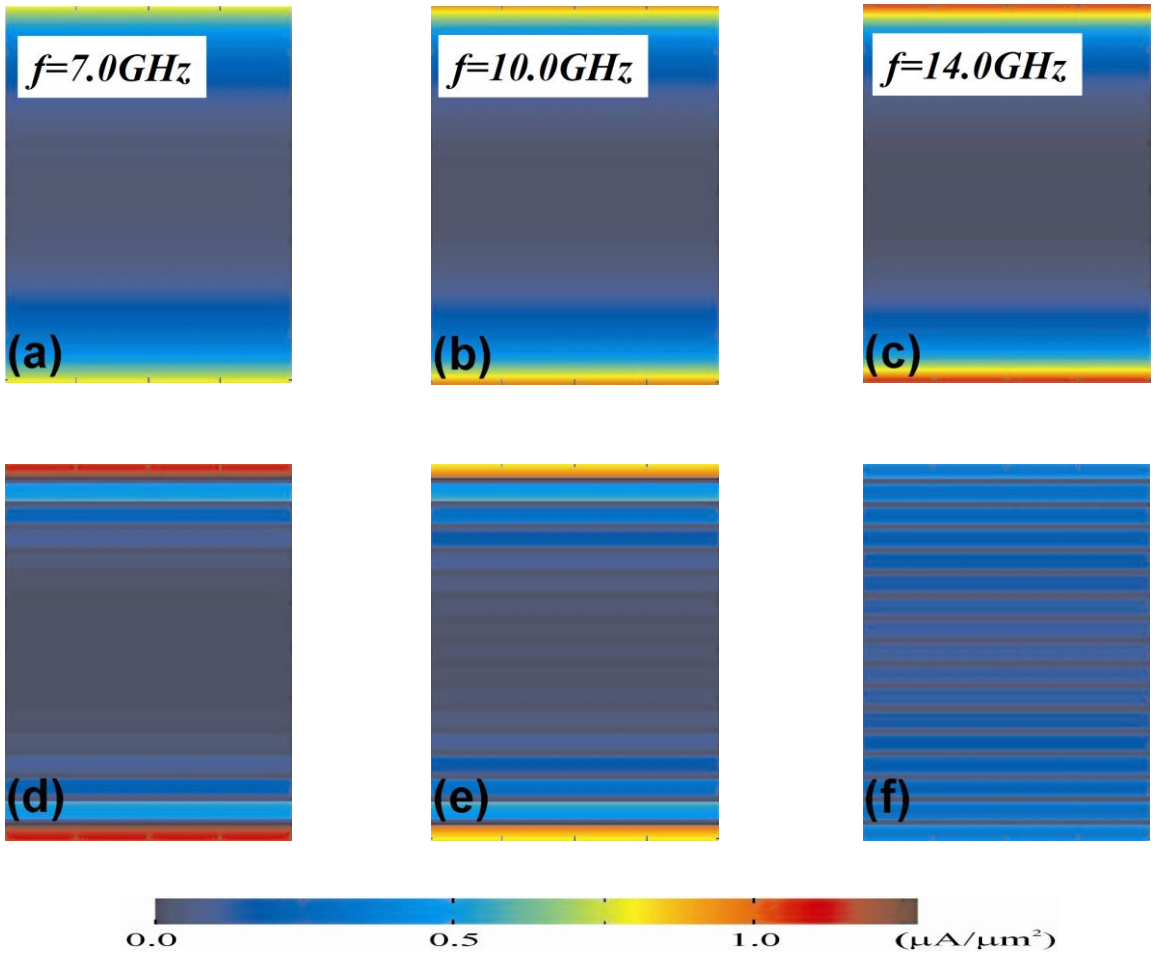

Figure 4.3.2: "Calculation of current distribution along the thickness in Cu (a, b, c) and ARLYM (d, e, and f) at three different frequencies (7, 10, and 14 GHz)" [42].

From the figure 4.3.2 we observe that for Copper conductor the skin effect causes the current to flow closer to the surfaces at top and bottom within the skin depth ' δ_{Cu} '.As the frequency increases this effect becomes less. In the case of ARLYM the current distribution also depends on the frequency. We see that at effective magnetic anti-resonant frequency of 14 GHz the current flows more uniformly as shown in the figure-4.3.2(f) which states that the suppression of

skin effect is at low frequency of about 10 GHz. In the above figure-4.3.2 at different frequencies of 7, 10 and 14 GHz the simulated current distribution is along the height of the conductors. Thus in all the three cases the current in Cu reference lines is concentrated on the top and bottom areas but the distribution of current in the lattice depends upon the frequency. At around the frequency of 7GHz the current density in ARLYM is concentrated at the top and bottom which indicates more non uniformity than the Copper reference lines shown in figure-4.3.2(a) and 4.3.2 (d). Similarly at frequency of 10 GHz we see the similar distribution of current which is shown in figures (fig-4.3.2(b) and fig-4.3.2(e)). The reason behind this is that the effective skin depth of the ARLYM and Copper can be compared at this frequency.

At the effective anti-resonant frequency at 14 GHz the current density spreads in all the copper layers as shown in figure-4.3.2(f). Thus the current is distributed more uniformly than the copper line (Figure-4.3.2(c)).

4.3.3 Device characterization:-

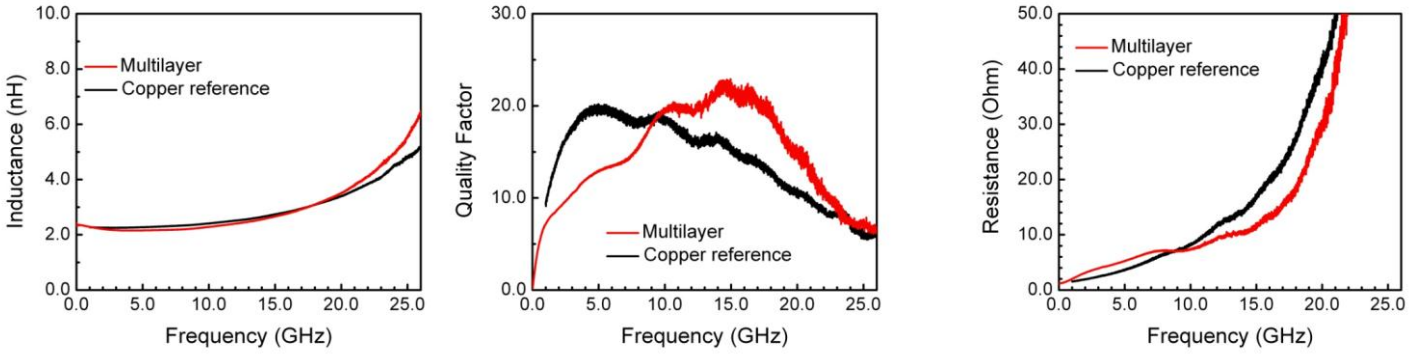

Figure 4.3.3: "Measured inductances (a), resistances (b), and quality factors (c) of a single turn spiral inductor made of pure copper – S22-ref (the black curves) and NiFe/Cu multi-layers – s22 (the red curves)" [42].

The above figure (fig-4.3.3) shows the plot for inductance (fig-4.3.3(a) [42]), Quality factor (fig-4.3.3 (b) [42]) and resistance (fig-4.3.3 (c) [42]) shown with respect to the frequency for each

individual copper reference and multilayer superlattice. We expect the resistance increasing monotonically with respect to the frequency due to the skin effect which is observed in the measurement for Cu S22 reference inductor. But we see a steep plateau between frequencies 10-18 GHz instead of increasing linearly in multilayer inductor. Therefore, in these frequencies the slope of resistance increase will be less than copper reference S22. We can neglect the induced losses as both the devices were fabricated on the same substrate (AF-45 glass). Thus, we can conclude from this that the decrease in the resistance is due to the skin effect suppression. On the other hand we can also state that the skin effect can be minimized or suppressed when the magnetic permeability goes to zero. From the figure 4.3.3 (a) we note that the inductance curve remains constant for the entire frequency range. The increase in the resistance also leads to higher quality factor as the frequency increases shown in fig-4.3.3 (b) [42]. From the fig-4.3.3 (b) [42] we notice that the quality factor value achieved is greater than 20 around 14 GHz [39]. As the resistance of the device S22 reduces to ~30 percent then the quality factor is increased to ~40 percent. From the figure 4.3.3 (c) we notice that at low frequencies < 7 GHz the resistance of the multilayer is greater that the simulated devices having the same configuration. The magnetic permeability for NiFe film is high at low frequency range which indeed leads to high eddy current loss when compared to the Cu film. But at frequencies above 18 GHz the resistance and quality factor get dominated by the LC resonance. Therefore, the effective bandwidth for skin effect suppression for NiFe/Cu multilayer is attained at 7-18GHz.

We expected that the ARLYM based inductors will attain high quality factor but we had problem with etching the devices. The values are listed in the table-4.2.1 where the actual line width '*w* 'of the devices was less than the actual values. The lowest conductor loss and partial skin effect suppression has been achieved at anti-resonance frequency ' f_{EAR} ' at large range. The

results obtained can be applicable to devices requiring the bandwidth such as clock signals in a microprocessor. The effective anti-resonance frequency can also be tuned by adjusting the thickness of each layer of NiFe and Cu. But the application of ARLYM can be only applied to the frequency range $f_{FMR} < f < f_{AR}$ where the real part of magnetic permeability is negative. Thus, the above range is defined by the ferromagnetic films between several GHz to about 30 GHz for $Ni_{80}Fe_{20}$. Therefore, if we try to use magnetic films with high saturation then $Ni_{80}Fe_{20}$ shifts the application frequency ' f_{AR} ' to high values.

4.3.4 Dependence of anti-magnetic resonance frequency:

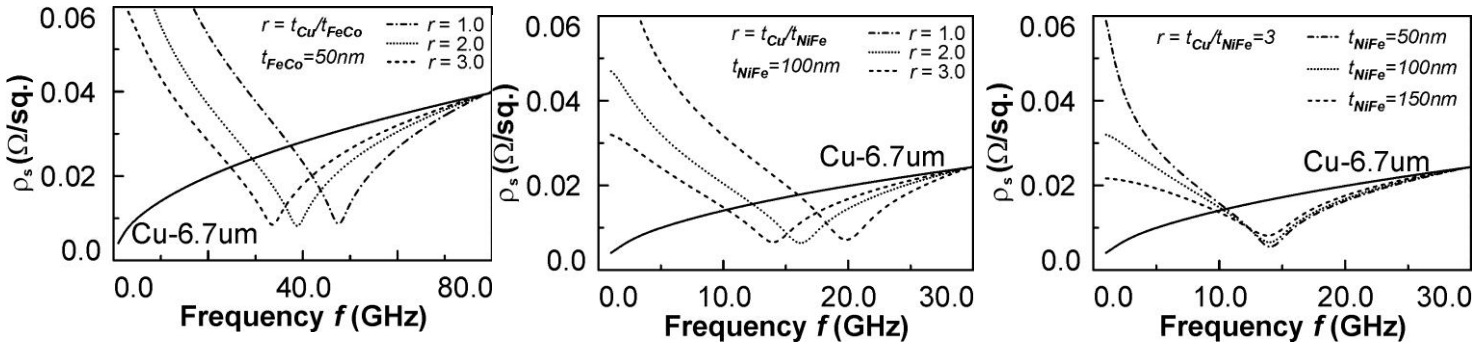

Figure 4.3.4: "(a) Calculated sheet resistance (ρ_s) of a 6.7 μm thick *NiFe/Cu* superlattices with (i) *r*=1.0, *N*=33, (ii) *r*=2.0, *N*=22, (iii) *r*=3.0, *N*=16. t_{cu}, and t_{NiFe}, are the thickness of the *Cu*, and NiFe layers, respectively. *N* is the number of superlattice period. The control *Cu CPW* with 6.7 μm thick was calculated for comparison. (b) Calculated ρ_s of a 6.7 μm thick *NiFe/Cu* superlattice with (i) t_{NiFe}=50nm, *N*=33 (ii) t_{NiFe}=100nm, *N*=16 (iii) t_{NiFe}=150nm, *N*=10. The thickness ratio *r* is fixed to 3. (c) Calculated sheet resistance of a 6.7 μm thick FeCo/Cu superlattice with (i) *r*=1.0, *N*=67, (ii) *r*=2.0, *N*=44, (iii) *r*=3.0, *N*=33. The thickness of the FeCo layer (t_{FeCo}) is kept to 50 nm" [42].

The figure above (Fig-4.3.4) shows the dependence of application frequency on the thickness ratio '*r*'. If the thickness ratio is small then it gives higher application frequency. If we try keeping the thickness ratio constant and dividing the bi-layers into fine thickness then we can reduce the losses. The plot obtained by keeping the thickness ratio '*r*' constant is shown in the

figure- 4.3.4 (b). Next if we replace $Ni_{80}Fe_{20}$ with high magnetization material 'M_0' such as FeCo having the magnetization value of ~2.4 T then the application frequency 'f_{AR}' can be increased as shown in the plot figure-4.3.4(c). The application frequency reaches maximum at approximately 67 GHz when the thickness ratio is approximately zero. Thus this is the maximum frequency for suppression of skin effect for high saturation magnetization materials. Therefore, this concept can be applicable to electronics and is fully compatible with CMOS technology. It can also be used for building components such as inductors, transmission lines etc, operating at high frequencies [42].

Bibliography:

1. Ian I., S. (2008). Impedance methods for electrochemical sensors using nanomaterials. TrAC Trends in Analytical Chemistry, 27(7), 604-611.
2. Iramnaaz, I., Sandoval, T., Zhuang, Y., Schellevis, H., & Rejaei, B. (2011). High quality factor RF inductors using low loss conductor featured with skin effect suppression for standard CMOS/BiCMOS. Electronic Components and Technology Conference (ECTC), 2011 IEEE 61st, 163-168.
3. Kim, Jungkyu, Junkin, Michael, Kim, Deok-Ho, Kwon, Seunglee, Shin, Young Shik, Wong, Pak Kin, & Gale, Bruce K. (2009). Applications, techniques, and microfluidic interfacing for nanoscale biosensing. Springer.
4. Kang, X., Wang, J., Wu, H., Aksay, I. A., Liu, J., & Lin, Y. (2009). Glucose Oxidase–graphene–chitosan modified electrode for direct electrochemistry and glucose sensing. Biosensors and Bioelectronics, 25(4), 901-905.
5. D. Rytting. "Network analyzer error models and calibration methods." White Paper, September 1998, Hewlett-Packard Company.
6. Kang, I., Heung, Y. Y., Kim, J. H., Lee, J. W., Gollapudi, R., Subramaniam, S., . . . Ruggles-Wren, M. (2006). Introduction to carbon nanotube and nanofiber smart materials. Composites Part B: Engineering, 37(6), 382-394.
7. Morgen, M., Ryan, E. T., Zhao, J.-H., Hu, C., Cho, T., & Ho, P. S. (January 01, 2000). Low Dielectric Constant Materials for ULSI Interconnects. Annual Review of Materials Science, 30, 645-680.

8. Viswanathan, S., & Radecki, J. (January 01, 2008). Nanomaterials in electrochemical biosensors for food analysis - a review. Polish Journal of Food and Nutrition Sciences, 58, 157-164.
9. Reyes, S. (January 01, 2005). De-embedding Using a Vector Network Analyzer Including Calibration and Measurement Techniques - Use of a software program and calibration system to automate the de-embedding process of removing adapter error contributions. Microwave Journal, 48, 3, 64.
10. Ansari, A. A., Alhoshan, M., Alsalhi, M. S., & Aldwayyan, A. S. (July 07, 2010). Prospects of Nanotechnology in Clinical Immunodiagnostics. Sensors, 10, 7, 6535-6581.
11. Kim, Jungkyu, Junkin, Michael, Kim, Deok-Ho, Kwon, Seunglee, Shin, Young Shik, Wong, Pak Kin, & Gale, Bruce K. (2009). Applications, techniques, and microfluidic interfacing for nanoscale biosensing. Springer.
12. AhammadLeeRahman, A. J. SalehJae-JoonMd. Aminur. "Electrochemical Sensors Based on Carbon Nanotubes." Sensors, v. 9 issue 4, 2009, p. 2289.
13. Hong Li, Wen-Yan Yin, Banerjee, K., & Jun-Fa Mao. (2008). Circuit modeling and performance analysis of multi-walled carbon nanotube interconnects. Electron Devices, IEEE Transactions on, 55(6), 1328-1337.
14. DanielsPourmand, Jonathan S.Nader. "Label-Free Impedance Biosensors: Opportunities and Challenges." Electroanalysis, v. 19 issue 12, 2007, p. 1239.
15. Kang, X. "Glucose Oxidase-graphene-chitosan modified electrode for direct electrochemistry and glucose sensing." Biosensors and Bioelectronics, v. 25 issue 4, 2009, p. 901.

16. Liu, M., Wen, Y., Li, D., Yue, R., Xu, J., & He, H. (2011). A stable sandwich-type amperometric biosensor based on poly (3, 4-ethylenedioxythiophene)–single walled carbon nanotubes/ascorbate oxidase/nafion films for detection of L-ascorbic acid. Sensors and Actuators B: Chemical, 159(1), 277-285.
17. Ito. "A Simple Through-Only De-Embedding Method for On-Wafer S-Parameter Measurements up to 110 GHz." IEEE MTT-S International Microwave Symposium digest. IEEE MTT-S International Microwave Symposium,, 2008, p. 382-385.
18. Suni, II. "Impedance methods for electrochemical sensors using nanomaterials." Trends in analytical chemistry: TRAC, v. 27 issue 7, 2008, p. 604.
19. Wang, Joseph. "Carbon-Nanotube Based Electrochemical Biosensors: A Review." Electroanalysis, v. 17 issue 1, 2005, p. 7.
20. Wu, JF. "Graphene-based modified electrode for the direct electron transfer of Cytochrome c and biosensing." Electrochemistry Communications, v. 12 issue 1, 2010, p. 175.
21. Dalmay, C., Pothier, Arnaud, Cheray, M., Blondy, P., Lalloue, F., & Jauberteau, M. O. (n.d.). On-chip biosensors based on microwave detection for cell scale investigations. (Communications in Computer and Information Science.)
22. Brownson, DAC. "An overview of graphene in energy production and storage applications." JOURNAL OF POWER SOURCES,, 2011.
23. Aizawa, H., Tozuka, M., Kurosawa, S., Kobayashi, K., Reddy, S. M., & Higuchi, M. (2007). Surface plasmon resonance-based trace detection of small molecules by competitive and signal enhancement immunoreaction. Analytica Chimica Acta, 591(2), 191-194.

24. Lu, R. (2003). CMOS low noise amplifier design for wireless sensor networks: Research project.
25. Merkoçi, A., Ambrosi, A., de la Escosura-Muñiz, A., Pérez-López, B., Guix, M., Maltez, M., & Marin, S. (2006; 2000). Nanomaterials for electroanalysis. In Encyclopedia of analytical chemistry () John Wiley & Sons, Ltd.
26. Aguilera, Jaime, & Berenguer, Roc. (2003). Design and Test of Integrated Inductors for Rf Applications. Springer Verlag.
27. Lu, C.-H., Chen, X., Chen, G.-N., Yang, H.-H., & Zhu, C.-L. (June 15, 2009). A graphene platform for sensing biomolecules. Angewandte Chemie - International Edition, 48, 26, 4785-4787.
28. Bacher, R., & Goudsmit, S. (1934). Atomic energy relations. I. Phys.Rev.Physical Review, 46(11), 948-969.
29. Yan Zhuang, Rejaei, B., Schellevis, H., Vroubel, M., & Burghartz, J. N. (2008). Magnetic-multilayered interconnects featuring skin effect suppression. Electron Device Letters, IEEE, 29(4), 319-321.
30. BufordHamiltonHolian, Mary CRaymond FAndrij. "A comparison of dispersing media for various engineered carbon nanoparticles." Particle and Fibre Toxicology, v. 4 issue 1, 2007, p. 6.
31. Wang, J. "Electrochemical biosensors: towards point-of-care cancer diagnostics." Biosensors and Bioelectronics, v. 21 issue 10, 2006, p. 1887.
32. Miura, N. "Highly sensitive and selective surface plasmon resonance sensor for detection of sub-ppb levels of benzo [a] pyrene by indirect competitive immunoreaction method." Biosensors and Bioelectronics, v. 18 issue 7, 2003, p. 953.

33. Li, R. C.-H. (2009). RF circuit design. Hoboken, N.J: Wiley.

34. Tsay, R. S. (2005). Analysis of financial time series. Hoboken, N.J: Wiley.

35. Iramnaaz, I., Sandoval, T., Zhuang, Y., Schellevis, H., & Rejaei, B. (2011). High quality factor RF inductors using low loss conductor featured with skin effect suppression for standard CMOS/BiCMOS. Electronic Components and Technology Conference (ECTC), 2011 IEEE 61st, 163-168.

36. NygaardHansen, SamuelsenAlberg, MarioaraLovik, U. C. S. D. (2009). Single-Walled and Multi-Walled Carbon Nanotubes Promote Allergic Immune Responses in Mice. Toxicological Sciences, 109(1), 113.

37. H. Ito and K. Masu, "A simple through only μ de embedding method for on wafer s parameter measurements up to 110 GHz," in IEEE MTT-S International Microwave Symposium Digest, June. 2008, pp. 383-386.

38. Iramnaaz, I., Xing, Y., Xue, K., Zhuang, Y., & Fitch, R. (2011). Graphene based RF/microwave impedance sensing of DNA. Electronic Components and Technology Conference (ECTC), 2011 IEEE 61st, 1030-1034.

39. Magnetic-multilayered interconnects featuring skin effect suppression
Y. Zhuang, B. Rejaei, H. Schellevis, M. Vroubel, J.N. Burghartz, IEEE Electron Device Lett. Volume: 29, Issue: 4, 2008, pp. 319-321.

40. B.C. Choi, Y.K. Hong, A. Lyle and G.W. Donohoe, “CMOS-based Spin-Transfer Torque Magnetic Random Access Memory (ST-MRAM)”, chapter in Nano-CMOS Memory Technology, CRC Press, 2009.

41. MabroukBoujemâaNdagijimanaBenechGhazel, MM AFPA. “Piezoelectric resonators for RF and microwave filters.” IOP Conference Series*:* Materials Science and Engineering, v. 13, 2010, p. 012011.

42. Iramnaaz I., Sandoval T., Zhuang Y., Schellevis H., Rejaei B., & 2011 61st Electronic Components and Technology Conference, ECTC 2011. (2011). High quality factor RF inductors using low loss conductor featured with skin effect suppression for standard CMOS/BiCMOS. Proc Electron Compon Technol Conf Proceedings - Electronic Components and Technology Conference, 163-168.

43. K.A Mkhoyan et al, Atomic and Electronic Structure of Graphene-Oxide, Nano Lett. 9, 1058 (2009).

44. Wang, Joseph. “Glucose Biosensors: 40 Years of Advances and Challenges.” Electroanalysis, v. 13 issue 12, 2001, p. 983.

45. Behzad Rejaei, and Marina Vroubel, "Suppression of skin effect in metal ferromagnet superlattice conductors," J. Appl. Phys., vol. 96, pp. 6863-6686, 2004.

Publications:

1. Iramnaaz, I., Sandoval, T., Zhuang, Y., Schellevis, H., & Rejaei, B. (2011). High quality factor RF inductors using low loss conductor featured with skin effect suppression for standard CMOS/BiCMOS. Electronic Components and Technology Conference (ECTC), 2011 IEEE 61st, 163-168.
2. Iramnaaz, I., Xing, Y., Xue, K., Zhuang, Y., & Fitch, R. (2011). Graphene based RF/microwave impedance sensing of DNA. Electronic Components and Technology Conference (ECTC), 2011 IEEE 61st, 1030-1034.